COGOW©

CLIMATOLOGY OF GLOBAL OCEAN WINDS

User Manual

http://cioss.coas.oregonstate.edu/cogow

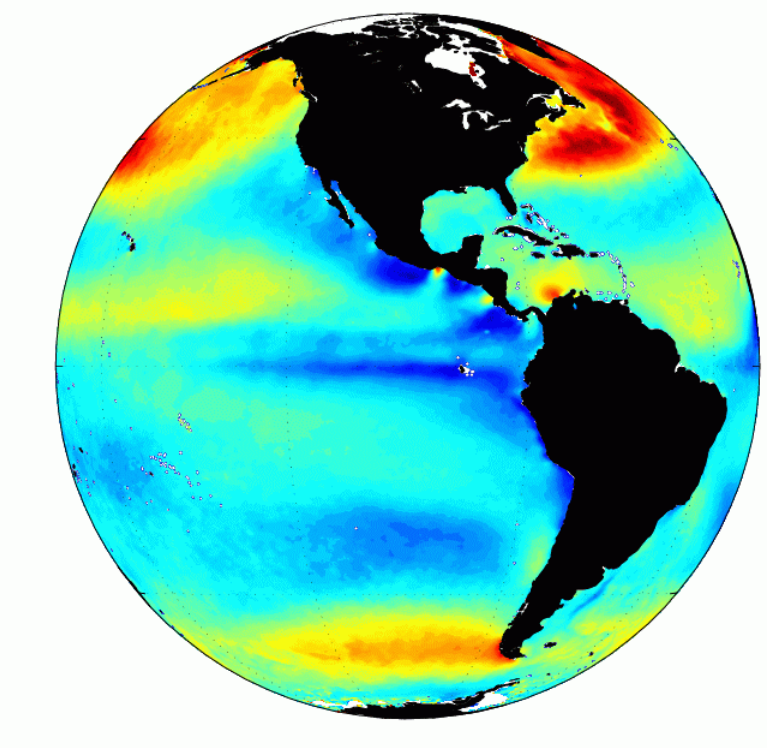

TABLE OF CONTENTS

Chapter 1: Introduction

Winds are the largest source of momentum for the upper ocean, affecting the full range of ocean movement, from individual surface gravity waves to complete current systems. Ocean winds modulate air-sea exchanges of heat, moisture, gases, and particulates. This modulation regulates the interaction between the atmosphere and the ocean, which establishes and maintains both regional and global climates.

Knowledge of the global wind field is therefore clearly desirable. This knowledge however has long been limited by poor *in situ* coverage by buoys and ships alike (Figure 1). The distribution of such observations is highly variable in time and space and as such is not adequate to truly resolve global ocean winds. Large portions of the tropics and the southern oceans are significantly under-sampled both temporally and spatially. Through high-resolution spatial sampling and frequent temporal sampling by satellites such as the National Aeronautics and Space Agency's (NASA) Quick Scatterometer (QuikSCAT), approximately 90 % of global ocean vector winds are now sampled daily at a 25 km resolution.

The Climatology of Global Ocean Winds (COGOW), presented here, is a web-based interactive atlas from which users can retrieve climatological wind maps as well as wind statistics, both in tabular and graphic form, on a 0.5° latitude by 0.5° latitude grid, for almost any particular region of interest. These wind statistics are based on five years (August 1999 – July 2004) of QuikSCAT measurements. The accuracy of QuikSCAT wind measurements is equivalent to that of observations by well-calibrated buoys. The global coverage of these QuikSCAT data provides valuable information about the wind statistics in the many regions of the world ocean that are sparsely sampled by ships and buoys. COGOW provides the first high spatial resolution, observationally based, online atlas of global ocean winds.

This manual proceeds as follows. Chapter 2 discusses the data and methods used in the creation of COGOW. Chapter 2 includes a brief description of scatterometry, a more detailed description of the QuikSCAT data that are included in this climatology, and a summary of data interpretation. In Chapter 3, a case study of NOAA (National Oceanic and Atmospheric Administration's) OR&R's (Office of Response and Restoration) involvement in the recovery of *Ehime Maru* is discussed to help familiarize users with COGOW and to illustrate just one of the potential uses of this product. A number of natural phenomena that are visible within COGOW are presented in Chapter 4 as potential starting points from which a user can begin to explore climatological global ocean wind fields. Chapter 5 contains a discussion of potential user groups. The final section, Chapter 6 presents a summary of this manual.

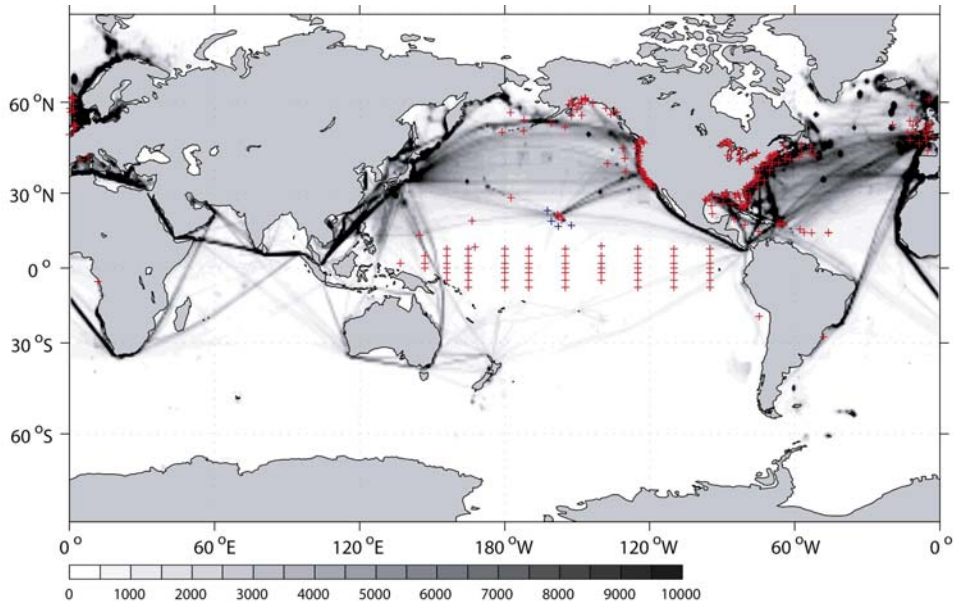

Figure 1. Total number of wind observations (January 1960 – December 1997) contained within the 1° x 1° Comprehensive Ocean-Atmosphere Data Set (COADS). The increment between gray shades is 500 observations. Note the Northern Hemisphere sampling bias in ship observations. The red crosses indicate buoys locations. The four blue crosses, in the vicinity of the Hawaiian Islands, indicate the locations of National Data Buoy Center (NDBC) buoys 51001, 51002, 51003, and 51004, discussed in Chapter 4. The data for all indicated buoys are available from the NDBC (http://www.ndbc.noaa.gov). Note the increased number of buoys in equatorial Pacific Ocean (the Tropical Atmosphere Ocean (TAO) array) and within U.S. and European coastal waters.

Chapter 2: Data and Methods

The data included in the Climatology of Global Ocean Winds (COGOW) are derived from the SeaWinds scatterometer that was launched on 19 June 1999 onboard the QuikSCAT satellite. The geophysical data record began on 15 July 1999. The 5-year data record presented here extends from 01 August 1999 through 31 July 2004. These data are freely available from Remote Sensing Systems as daily, 3-day, weekly and monthly averages on a 0.25° latitude by 0.25° longitude grid.

SeaWinds on QuikSCAT

The SeaWinds on QuikSCAT mission was a "quick recovery" mission to fill the gap created by the unexpected loss of the NASA Scatterometer (NSCAT) in June 1997 after only 9 months of operation. The polar orbiting QuikSCAT satellite is in a sun-synchronous orbit, 803km above the earth's surface. With an orbit period of 101 minutes, QuikSCAT is able to sample about 90% of the global oceans daily (Schlax *et al*., 2001). As a result of side lobe contamination, standard QuikSCAT measurements cannot be obtained within 30 km of land.

The SeaWinds scatterometer is a scanning microwave radar that uses electromagnetic backscatter from the wind roughened ocean surface at multiple antenna look angles to infer surface wind stress magnitude and direction (Freilich *et al*., 1994; Chelton and Freilich, 2005). The geophysical product of the scatterometer is calibrated to the equivalent neutral-stability wind, 10-m above the sea surface, and vector averaged onto a 0.25° latitude by 0.25° longitude grid. For a given wind stress at the sea surface, the equivalent neutral stability wind is the wind that would exist at a height of 10 m if the atmosphere were neutrally stable.

The accuracy of the QuikSCAT wind retrievals is best characterized in terms of random component errors (Freilich and Dunbar, 1999). In an analysis that extends the

isotropic random component error model of Freilich (1997) and Freilich and Dunbar (1999) to include anisotropy, Vanhoff and Freilich (2004, unpublished manuscript) conclude that QuikSCAT data have random component error magnitudes of about 0.75 $m.s^{-1}$ in the along-wind direction and 1.50 $m.s^{-1}$ in the crosswind direction. Assuming the component errors are uncorrelated, the wind speed accuracy is therefore about 1.68 $m.s^{-1}$ at all wind speeds. Wind direction accuracy increases significantly with increasing wind speed. For a 6 $m.s^{-1}$ wind, the anisotropic component errors correspond to a directional accuracy of about 14° (Chelton and Freilich, 2005).

For more detailed discussions of scatterometry and the issues involved in the sampling of scatterometer, data the reader is referred to Chelton and Freilich (2005) and Schlax *et al*. (2001), respectively.

Data Usage

Monthly Composite Maps

The time averaged monthly composites are scalar and vector averaged for wind speed and wind direction respectively. In the example shown in Figure 2, the colors represent wind speed in knots (1 knot ≈ 0.5 $m.s^{-1}$) plotted on a 0.25° latitude by 0.25° longitude grid. The vector averaged climatological wind directions are plotted as unit vectors in the regional map (top panel) on a 1° latitude by 1° longitude grid. In the sub-regional maps (four lower panels), vector averaged climatological wind directions are plotted as unit vectors on a 0.5° latitude by 0.5° longitude grid. Each of these four panels overlaps adjacent panels by 10° of latitude and 20° of longitude.

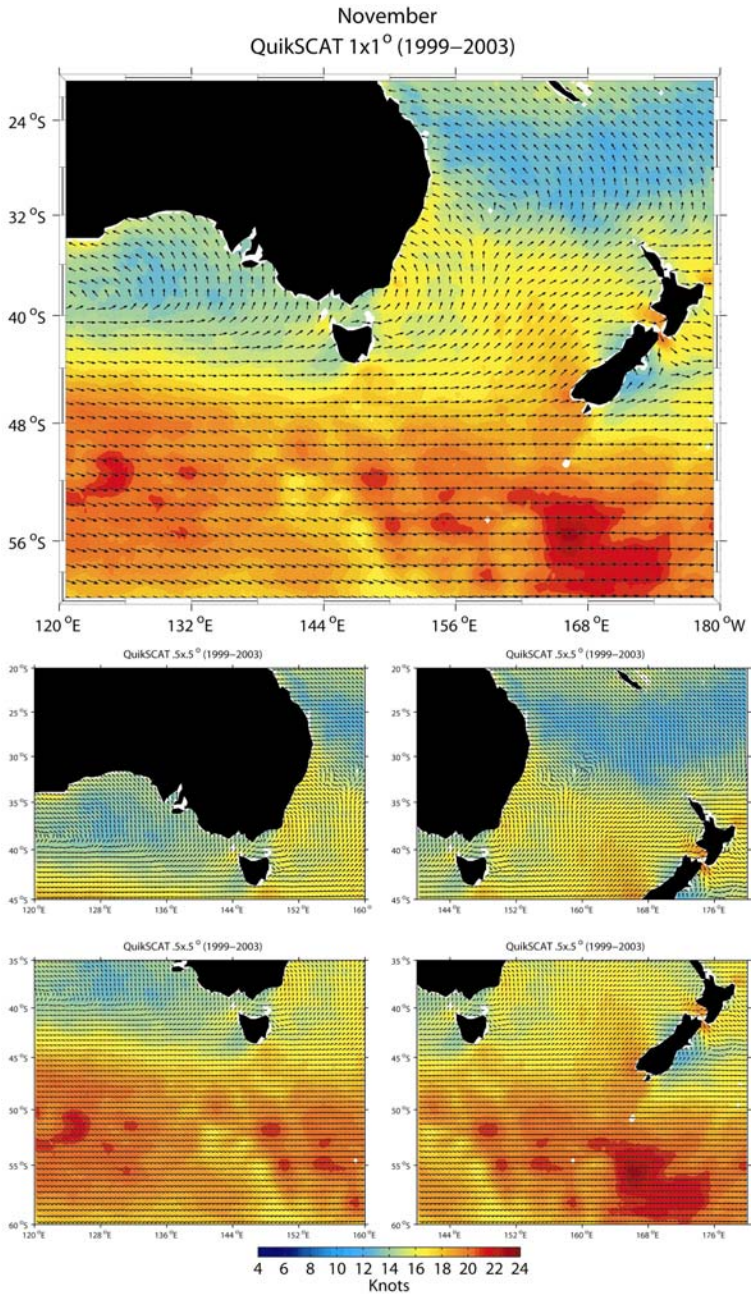

Figure 2. November composite average (1999-2003) of the wind field at 10 m derived from the QuikSCAT scatterometer. Scalar averaged wind speed is shown in color on a 0.25° x 0.25° grid. Vector averaged climatological wind directions are plotted, as unit vectors, in the top panel (or regional map) on a 1° x 1° grid. In the four lower panels vector averaged climatological wind directions are plotted, as unit vectors, on a 0.5° x 0.5° grid. Each of the four lower panels (or sub-regional maps) overlaps adjacent panels by 10° of latitude and 20° of longitude.

Wind Roses

The wind rose plots presented in COGOW are created from temporally and spatially smoothed QuikSCAT wind fields. These wind fields are temporally averaged from a daily interval to a 3-day interval. For example, the wind field for 1 January is a composite of the wind fields for 30 December through 1 January. Similarly, the wind field for 2 January is a composite of the wind fields for 31 December through 2 January. January therefore contains 31, temporally averaged, "daily" wind fields. A spatial smoothing of 0.5° latitude by 0.5° longitude is also applied. The 3-day temporal averaging (Figure 3) is applied because QuikSCAT wind fields are somewhat gappy at daily time scales as a result of both QuikSCAT's uneven sampling in time and space (Figure 4) and data loss from rain contaminated wind retrievals. The 0.5° latitude by 0.5° longitude spatial averaging is applied to reduce data density.

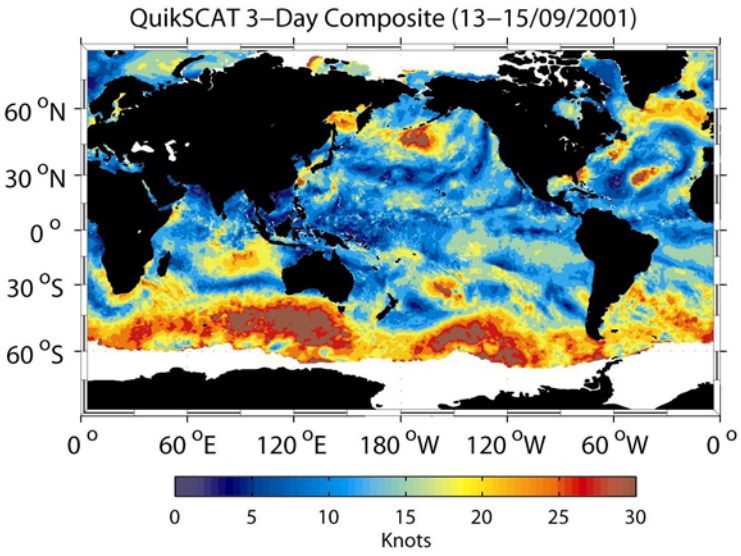

Figure 3. An example three-day composite average of ocean wind speeds at a 10 m height over 0.25° x 0.25° areas derived from the QuikSCAT scatterometer over the 3-day period 13-15 September 2001.

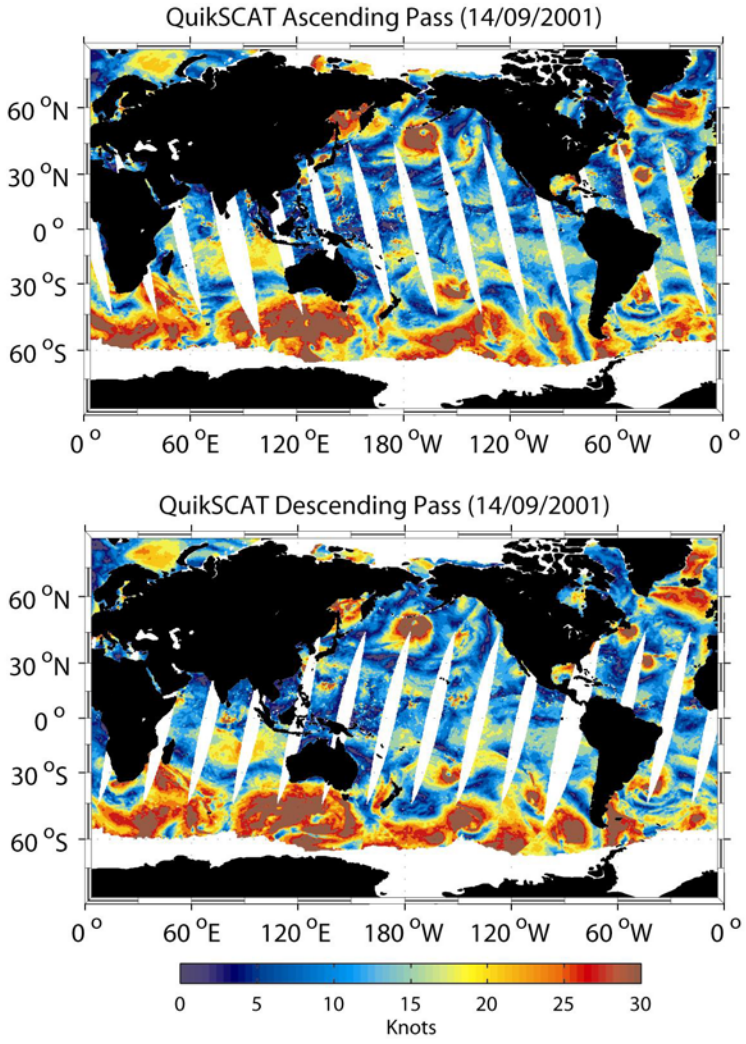

Figure 4. Daily (14 September 2001) ascending orbit segments (local morning passes) (top panel) and descending orbit segments (local evening passes) (bottom panel) of ocean wind speeds at a 10 m height over 0.25° x 0.25° areas derived from the QuikSCAT scatterometer.

The temporally and spatially averaged observations are sorted into 6 wind speed bins with lower limits of, 0, 5, 10, 15, 20 and 25 knots, and 16 non-overlapping directional bins of width 22.5° so that, for example, the "north" bin includes events with direction from 11.25° west of north to, but not including, 11.25° east of north. The wind direction is defined by the meteorological convention as the direction the winds are blowing from.

Wind roses (Figure 5) summarize the occurrence of overlapping 3-day average winds within a 0.5° latitude by 0.5° longitude bin centered at 39.75°N 125.75°W, showing their strength, direction and relative frequency. The wind rose is interpreted as follows: the length of the barbs that extend radially from the center of the rose, reflect each direction's relative frequency. If the barb pointing from the north-northwest is twice as long as the barb pointing from the north, then the winds blew FROM the north-northwest twice as frequently as they did from the north.

In each direction, the barb's appearance varies through several styles in sequence. The proportion of the barb's length in each style indicates the proportion of time winds blew from that direction at a given speed. For example, a thin, light gray rectangle extending from the centre indicates wind speeds of between 0 and 5 knots. A slightly thicker, and slightly darker gray, segment indicates wind speeds of between 5 and 10 knots, and so forth until, finally, a thick black rectangle indicates wind speeds greater then 25 knots. To aid with interpretation, concentric rings at 20 % frequency intervals are plotted on each wind rose. Additionally, the total number of overlapping 3-day average observations used to create each wind rose is included in the lower right-hand-corner of each plot.

For the month of July (Figure 5) the winds in the 0.5° x 0.5° bin centered at 39.75°N 125.75°W blew from the north-northwest and from the north for 58.44 and 31.82 % of the time respectively. The winds that blew from the north-northwest did so at speeds between 15 and 20 knots for about 30 % of the time, twice as frequently as north-northwest winds with speeds between 20 and 25 knots (Table 2). Appendix B shows the raw data used to create both Figure 5 and Table 2. Appendix B is an example of the format that the raw wind data for all other months and locations are presented in, i.e. each comma delimited (*.csv) ASCII text file contains a two line header that gives the date and location, and three columns of data: dd/mm/yy, wind speed and wind direction. Missing data are reported as NaN's (Not a Number). The

*.csv file format can be imported into spreadsheet applications such as Microsoft Excel with relative ease.

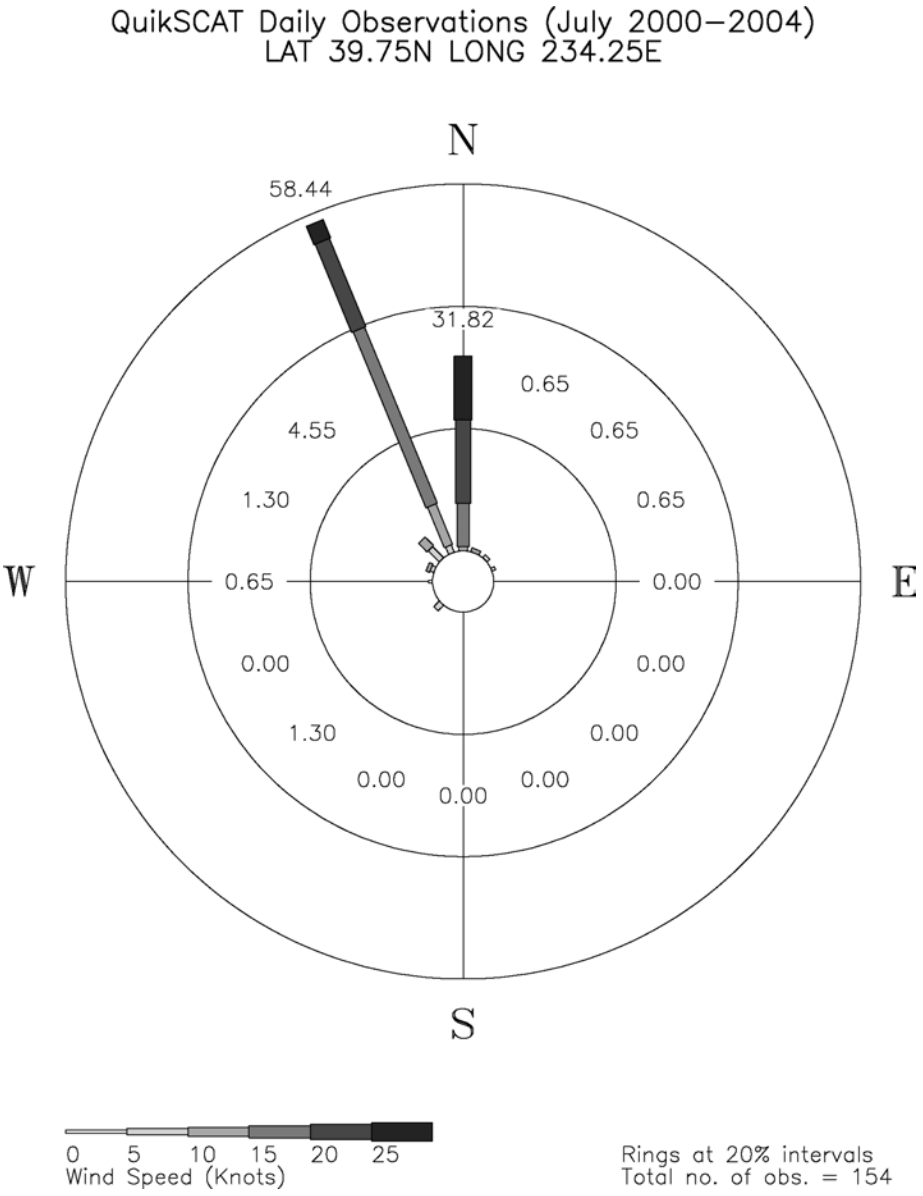

Figure 5. Wind rose plot for the month of July (2000-2004) for a 0.5° x 0.5° area centered at 39.75°N and 125.75°W off the coast of northern California. See Table 2 for the tabular form of this wind rose plot and Appendix B for the raw data used to create this plot.

Table 1. Tabular form of the July data presented graphically in Figure 5.

Wind Direction vs Speed from QuikSCAT Daily Observations (July 2000-2004)							
LAT 39.75N LONG 234.25E							
Total Number of Observations = 154							
Wind Spd (knots)	0.0 <=	5.0 <=	10.0 <=	15.0 <=	20.0 <=	25.0 <	Total
Meteorological Wind Dir							Percent
N	0.00	0.00	0.65	7.14	13.64	10.39	31.82
NNE	0.00	0.00	0.65	0.00	0.00	0.00	0.65
NE	0.00	0.65	0.00	0.00	0.00	0.00	0.65
ENE	0.65	0.00	0.00	0.00	0.00	0.00	0.65
E	0.00	0.00	0.00	0.00	0.00	0.00	0.00
ESE	0.00	0.00	0.00	0.00	0.00	0.00	0.00
SE	0.00	0.00	0.00	0.00	0.00	0.00	0.00
SSE	0.00	0.00	0.00	0.00	0.00	0.00	0.00
S	0.00	0.00	0.00	0.00	0.00	0.00	0.00
SSW	0.00	0.00	0.00	0.00	00.0	0.00	0.00
SW	0.00	1.30	0.00	0.00	0.00	0.00	1.30
WSW	0.00	0.00	0.00	0.00	0.00	0.00	0.00
W	0.65	0.00	0.00	0.00	0.00	0.00	0.65
WNW	0.00	0.65	0.65	0.00	0.00	0.00	1.30
NW	0.00	2.60	1.95	0.00	0.00	0.00	4.55
NNW	0.00	1.30	7.14	31.17	15.58	3.25	58.44
Total Percent	1.30	6.49	11.04	38.31	29.22	13.64	100.00

Chapter 3: Climatology of Global Ocean Winds (COGOW)

An Introduction to COGOW

The climatology of Global Ocean Winds (COGOW) is a publicly available 5-year climatology of global ocean wind speed and direction. This web-based interactive atlas, which is accessible at URL http://cioss.coas.oregonstate.edu/cogow, allows users to retrieve scatterometer-derived wind statistics, in both tabular and graphic form, for a particular region of interest on 3-day and monthly timescales and on a 0.5° latitude by 0.5° longitude grid. While this climatology is accessible via almost all web browsers, it is best viewed at a screen resolution of 1600x1200 DPI (dots per inch) using Mozilla-branded browsers[1] (Mozilla and Firefox) or later versions of Netscape (Netscape 8), all of which are based on the open source web browser layout engine known as Gecko[2]. The above screen resolution was adopted as a compromise between website design/layout and monthly composite map visualization (Figure 2). This climatology is not optimized for lower-resolution computer monitors.

Learning the Basics

The case study below details NOAA OR&R's involvement in the recovery efforts of *Ehime Maru*. This case study serves to familiarize users with COGOW and is just one of the potential uses of this product.

Background to the *Ehime Maru* Recovery Operation

On 9 February, 2001, USS *Greeneville*, a Los Angeles class submarine, collided with *Ehime Maru*, a Japanese training and fishing vessel, approximately 17 km south of

[1] http://www.mozilla.org/
[2] Minor technical problems occur with Microsoft Internet Explorer 6 Service Pack 1, as summarized below in the discussion of Figure 13.

Diamond Head on the island of Oahu, Hawaii. *Ehime Maru* sank in about 600 meters of water. At the time of sinking, 26 of the 35 crewmembers were rescued. The US Navy was unable to locate the nine remaining crewmembers. It was presumed that they were trapped inside the vessel or went overboard as the ship sank. Following communications with the Japanese government, the US Navy agreed to attempt to recover *Ehime Maru* crewmembers, their personal effects, and certain unique characteristic ship components (Department of the Navy, 2001).

Prior to this recovery effort, the US Navy was required by the mandates of the National Environmental Policy Act (NEPA) of 1969 to prepare an environmental assessment (EA) that would evaluate the potential environmental effects of the U.S. Navy's proposal to lift *Ehime Maru* from the seafloor, transport the vessel to a shallow-water site in order to recover the crewmembers, and then permanently relocate the ship to a deep-water site (Department of the Navy, 2001). This EA resulted in a FONSI[3] (finding of no significant impact). Accordingly, a NEPA environmental impact statement (EIS) was not performed.

The EA resulted in the selection of Reef Runway, located to the southeast of Pearl Harbor, as the preferred shallow-water recovery site (Department of the Navy, 2001). Based on Reef Runway as the preferred shallow-water recovery site, NOAA OR&R ran a series of oil plume trajectory analyses to model the behavior of an uncontained diesel fuel release. Several variables were factored into the models before they were run, including release location, wind direction, time period, and tide conditions (ebb or flood). Constants included the wind speed (assumed to be 10 knots) and amount of diesel fuel released (76,000 liters) (Department of the Navy, 2001). NOAA OR&R's use of a 10 knot wind speed was based on the average wind speed recorded at the Honolulu International Airport in August over the previous 10 years (NCDC, 2001). The fuel release of 76,000 liters was considered to be the most realistic amount of diesel fuel that would be released. The models were run with a 90 % confidence limit

[3] http://www.smdcen.us/pubdocs/files/ehime_fonsi_final_061501.pdf

and as if the release occurred instantaneously as opposed to occurring over a period of time. The time period for every model run was 24 hours (Department of the Navy, 2001).

The results of the NOAA OR&R model runs are shown in Figures 6 and 7. These figures show that easterly winds would result in diesel fuel being pushed toward the beach at Barbers Point during both ebb and flood tide conditions. East-northeast winds could also potentially result in diesel fuel being pushed toward the beach during both ebb and flood tidal conditions; however, it appeared to be much more likely during flood conditions. North and northeast winds would result in the plume being pushed offshore after 24 hours in all conditions.

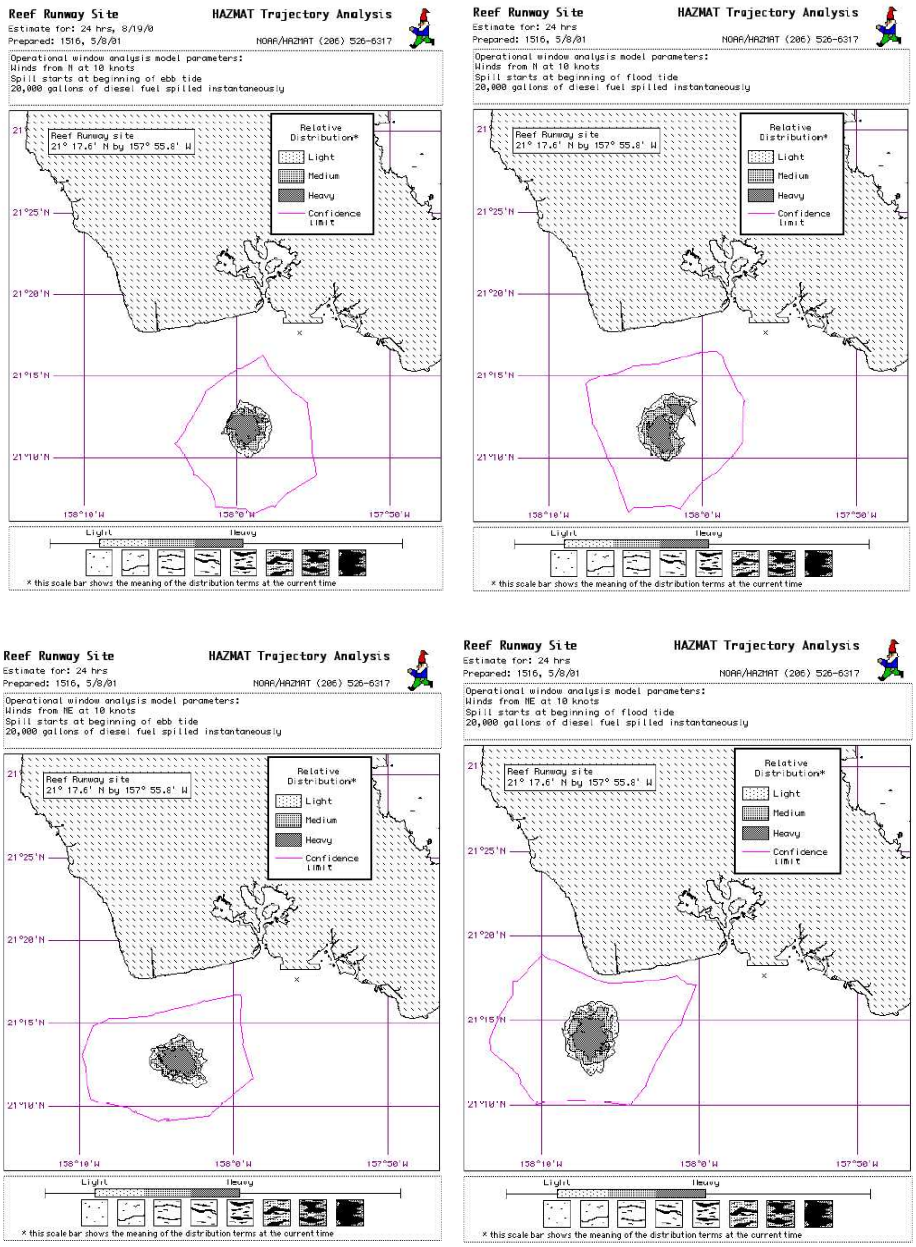

Figure 6. The NOAA OR&R trajectory analyses for the Reef Runway shallow-water recovery site, indicated by a cross to the southeast of Pearl Harbor. The top panels show the results of the ebb (left) and flood (right) tide analyses that were forced with a 10 knot northerly wind. The bottom panels show the results of the ebb (left) and flood (right) tide analyses that were forced with a 10 knot northeasterly wind. All analyses were run with a 90 % confidence limit, indicated by the purple line in each panel, and an instantaneous release of material. Regions of oil concentration (Light, Medium, and Heavy) are shaded. The time period for every analysis was 24 hours. (after Department of the Navy, 2001)

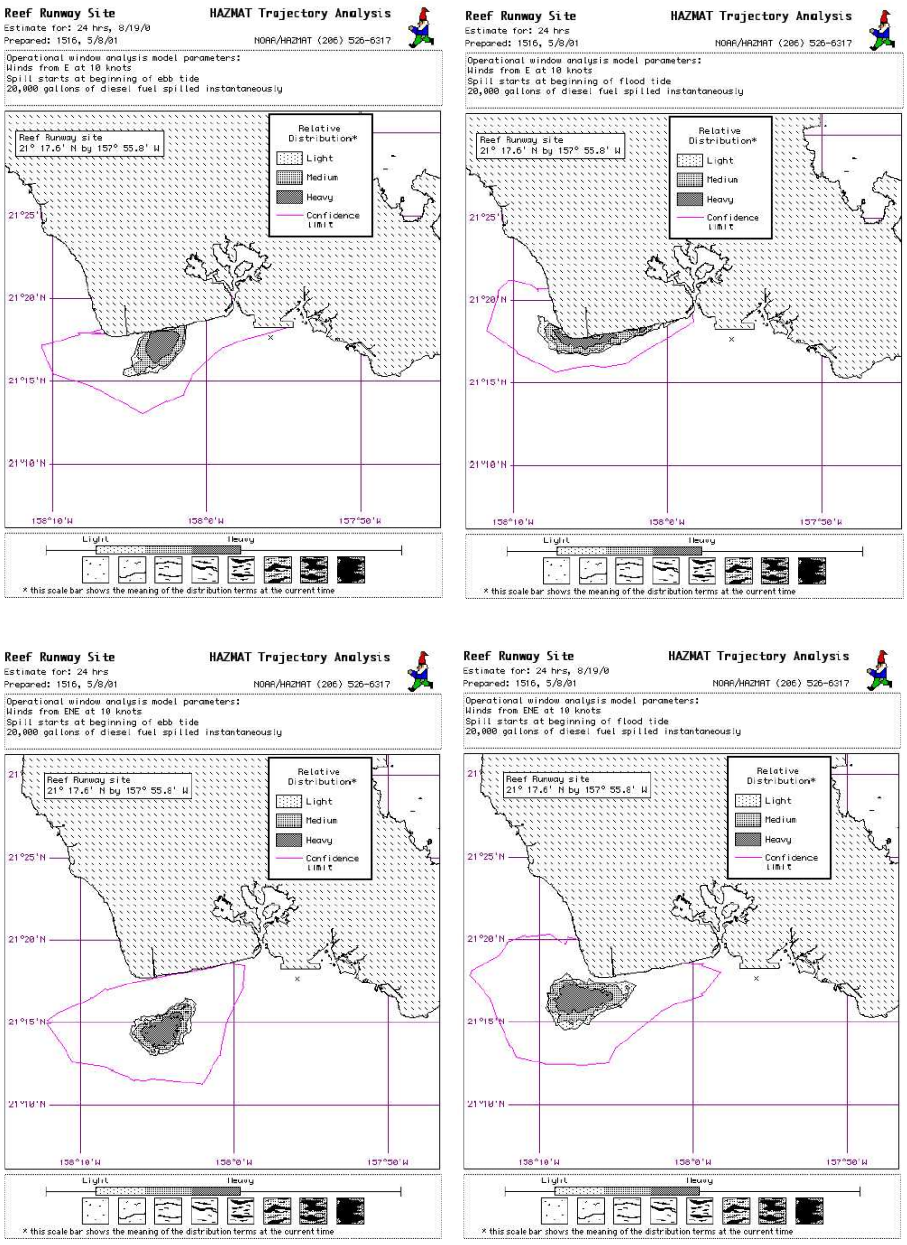

Figure 7. The same as Figure 6 except that the top panels show the results of the ebb (left) and flood (right) tide analyses that were forced with a 10 knot easterly wind. The bottom panels show the results of the ebb (left) and flood (right) tide analyses that were forced with a 10 knot east-northeasterly wind. (after Department of the Navy, 2001)

As mentioned above, NOAA OR&R's oil plume trajectory analyses were based on the average wind speed recorded at the Honolulu International Airport in August over the previous 10 years. The Honolulu International Airport weather station is located at 21.35°N 157.93°W, approximately 30 km from where *Ehime Maru* initially sank.

NOAA OR&R's use of the 10 year average August wind speed recorded at the Honolulu International Airport raises the following questions:

1. How representative is the assumed wind speed of 10 knots?
2. How variable is the wind field off the island of Oahu in terms of wind direction for the month of August?

To answer these questions, NOAA OR&R could have considered data derived from four National Data Buoy Center (NDBC) buoys 51001 (23.43°N 162.21°W), 51002 (17.14°N 157.79°W), 51003 (19.16°N 160.74°W), and 51004 (17.52°N 152.48°W), shown by the blue crosses in Figure 1. These buoys are, however all situated a considerable distance offshore of Oahu. It can therefore be argued that consideration of the buoy data would have been ineffectual with respect to the nearshore recovery effort of *Ehime Maru*. NOAA OR&R also had access to the National Centers for Environmental Predication (NCEP) operational wind fields (Kanamitsu, 1989). While these model fields have a reasonable temporal resolution of six hours and a grid resolution of 1° latitude by 1° longitude, the NCEP model is not able to resolve features with scales smaller than about 500 km (Milliff *et al*., 2004). The NCEP model therefore smears the small-scale local wind features that may be critical to oil plume trajectory modeling.

The following section details how access to the COGOW climatological wind atlas could have been useful in NOAA OR&R's modeling of a potential oil spill during this recovery operation.

Getting Started with COGOW

To begin, type the URL http://cioss.coas.oregonstate.edu/cogow into the address field of your preferred web browser.

Welcome to the homepage of the Climatology of Global Ocean Winds.

Contained within this homepage is a map of the Earth (Figure 8). If this image does not appear, it may be necessary to install Macromedia Flash Player. To do so type the following URL into your web browser address field:

> http://www.macromedia.com/shockwave/download/download.cgi?P1_Prod_Version=ShockwaveFlash.

To download the required plugins, left-click on the "Download Now" button and follow the installation instructions.

With Macromedia Flash Player correctly installed, the map of the Earth in Figure 8 should now be visible. This near-global map is divided into seventy-seven 40° latitude by 60° longitude regional maps. As the cursor is moved over the image, semi-transparent blue colored boxes appear, indicating the approximate locations of each of the aforementioned regional maps (Figure 8). As mentioned above, each regional map overlaps adjacent regional maps by 20° of latitude and 30° of longitude. Each overlapping regional map, depicting vector winds on a 1° latitude by 1° longitude grid, is subdivided into four overlapping sub-regional maps spanning 25° of latitude and 40° of longitude that depict vector winds on a 0.5° latitude by 0.5° longitude grid, as shown by the example in Figure 2.

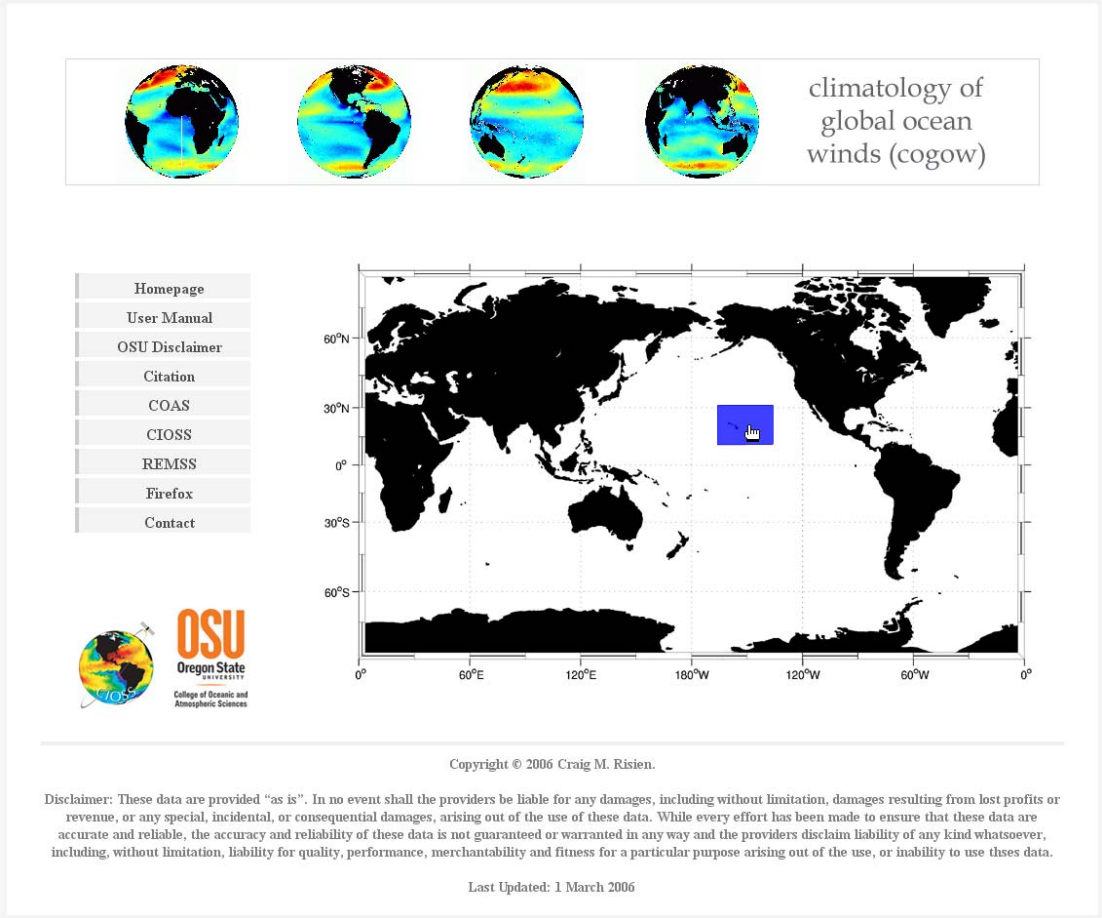

Figure 8. A screenshot of the homepage of the Climatology of Global Ocean Winds (http://cioss.coas.oregonstate.edu/cogow). The global map is subdivided into seventy-seven, overlapping (40° latitude by 60° of longitude) regional maps. Left click on any one of these regional maps to explore the five-year climatology of ocean winds derived from the QuikSCAT satellite.

For the purposes of demonstration, the wind field off the Hawaiian Islands is considered here.

Left-clicking on the region shown in Figure 8 displays the regional map shown in Figure 9 for the month of January (2000-2003).

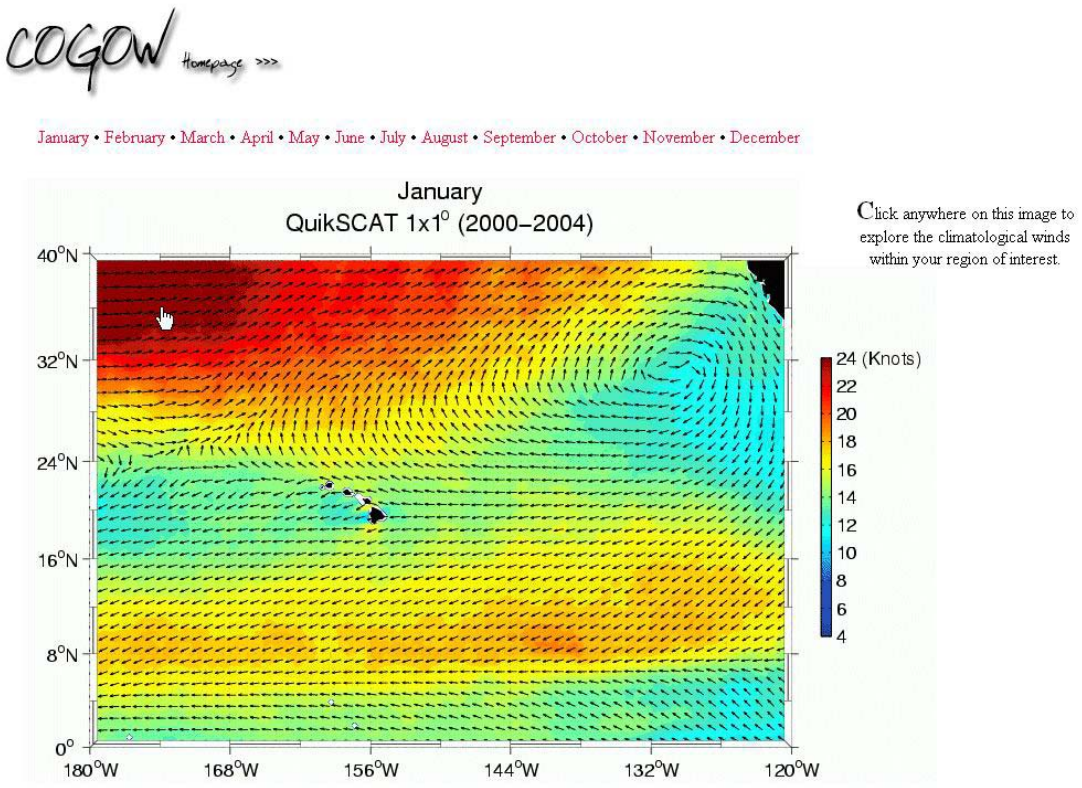

Figure 9. January composite average (2000-2004) of the wind field at 10 m derived from the QuikSCAT scatterometer. Scalar averaged wind speed is shown in color on a 0.25° x 0.25° grid. Vector averaged climatological wind directions are plotted as unit vectors on a 1° x 1° grid.

The climatological mean month-to-month variability observed in the 5-year QuikSCAT data for this region can be seen by left-clicking, in sequence, on each of the month tabs located directly above the regional maps.

The January through December climatological mean maps for the region centered on Hawaii are shown in Figures 10 and 11.

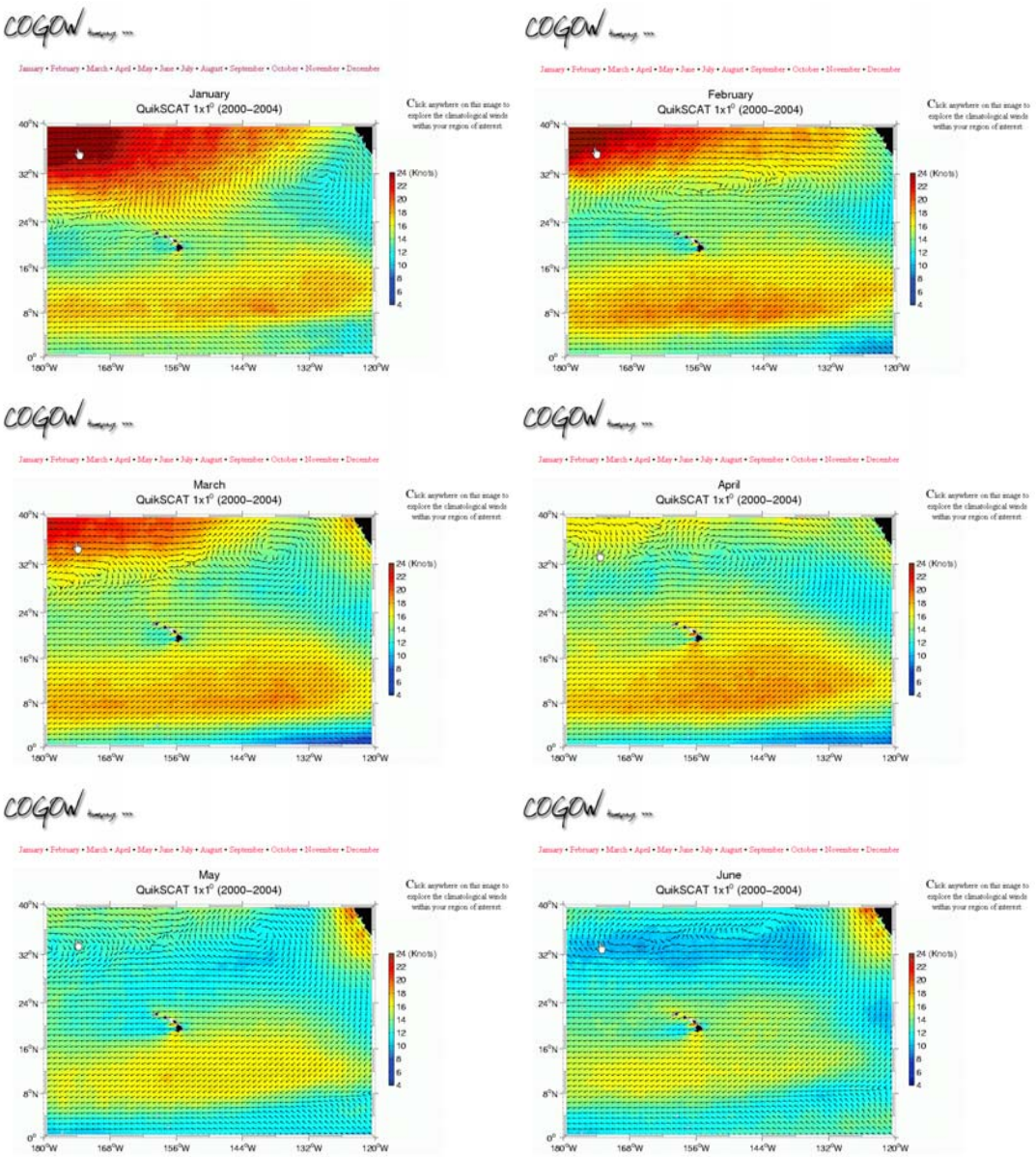

Figure 10. Composite averages of the wind field at 10 m derived from the QuikSCAT scatterometer for the month of January (top-left panel) through to June (bottom-right panel). Scalar averaged wind speed is shown in color on a 0.25° x 0.25° grid. Vector averaged climatological wind directions are plotted as unit vectors on a 1° x 1° grid.

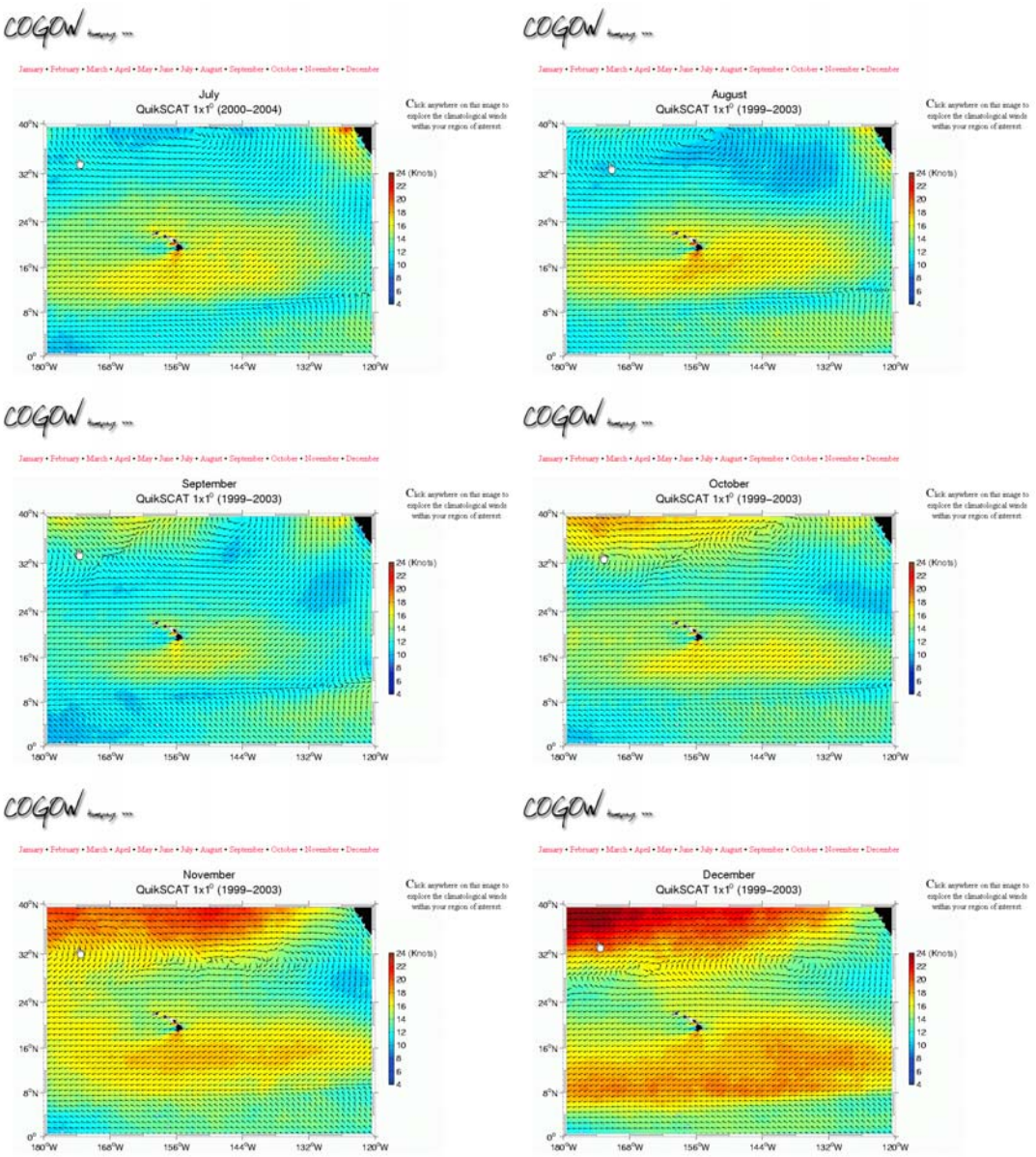

Figure 11. The same as Figure 10 except for the monthly composite for July (top-left panel) through to December (bottom-right panel).

The northward retreat of the westerly wind belt with the onset of the boreal spring and summer is evident from this sequence of maps. Commensurate with this retreat is the seasonal variation in latitude of the Inter-Tropical Convergence Zone (ITCZ)[4], located approximately between 0 and 9°N. The summer months of May through August show winds that are about 50 % weaker than those of the winter months. An exception to this can be seen in the top right corner over the California Current as well as in the Alalakeiki Strait that separates the islands of Hawai`i and Maui. The large-scale anticyclonic circulation that is associated with the North Pacific Subtropical High is also apparent. This feature is centered at about 40°N 150°W for the months of July and August.

Recall that NOAA OR&R's oil plume trajectory analyses shown in Figures 6 and 7 used the 10 year average August wind speed recorded at the Honolulu International Airport. The QuikSCAT climatological average wind field for this region can viewed by left-clicking on the "August" tab. This will display the regional map for the month of August shown in Figure 12. This regional map is subdivided into four sub-regional maps, or quadrants, which overlap each other by 10° latitude by 20° longitude, as shown in the lower four panels of Figure 2.

[4] The Inter-Tropical Convergence Zone (ITCZ) is an area of relatively low pressure that forms where the northeast trade winds meet the southeast trade winds just north of the Earth's equator. This band moves seasonally. It moves toward the equator for the austral summer (October - February) and toward the north for boreal summer (May - August). The ITCZ is, however less mobile over the oceanic longitudes, where it holds a more stationary position just north of the equator.

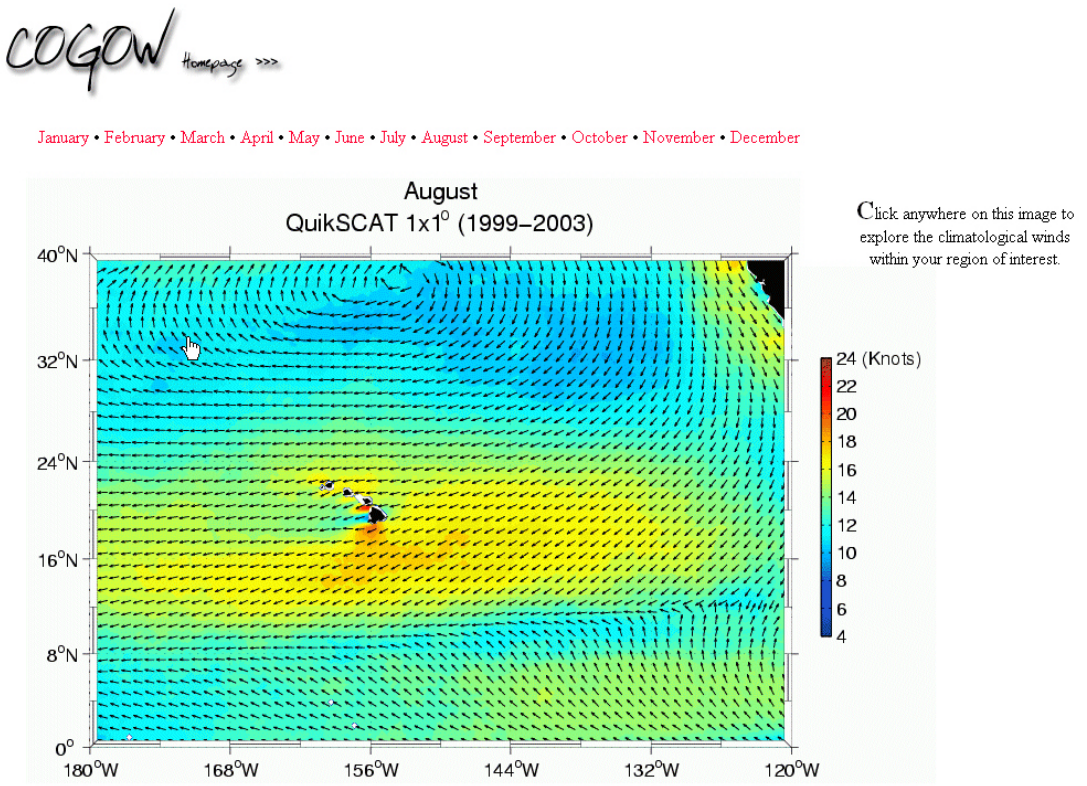

Figure 12. August composite average (1999-2003) of the wind field at 10 m derived from the QuikSCAT scatterometer. Scalar averaged wind speed is shown in color on a 0.25° x 0.25° grid. Vector averaged climatological wind directions are plotted as unit vectors on a 1° x 1° grid.

To zoom in on the Hawaiian Islands, left-click on a point near the sub-region of interest. The user will see the high-resolution sub-regional climatological mean map for the month of August shown in Figure 13.

For those users using the Microsoft Internet Explorer 6 Service Pack 1 browser a pop-up box will appear. This popup states, “A script on this page is causing IE to run slowly. If it continues to run, your computer may become unresponsive. Do you want to abort the script?” Select “no” to ignore this message and continue on. The reason for this pop up is that a substantial amount of JavaScript is used to render each sub-regional map. This rendering, which occurs every time one of these sub-regional maps is selected, takes about 10 seconds to complete. By adjusting Internet

Explorer's timeout value, the user can overcome this Microsoft limitation. This adjustment is achieved through a modification of the system registry. A detailed discussion of this procedure is give in this Microsoft knowledgebase article http://support.microsoft.com/?kbid=175500. This limitation is not found in the Mozilla-branded browsers (Mozilla and Firefox) or Netscape 8.

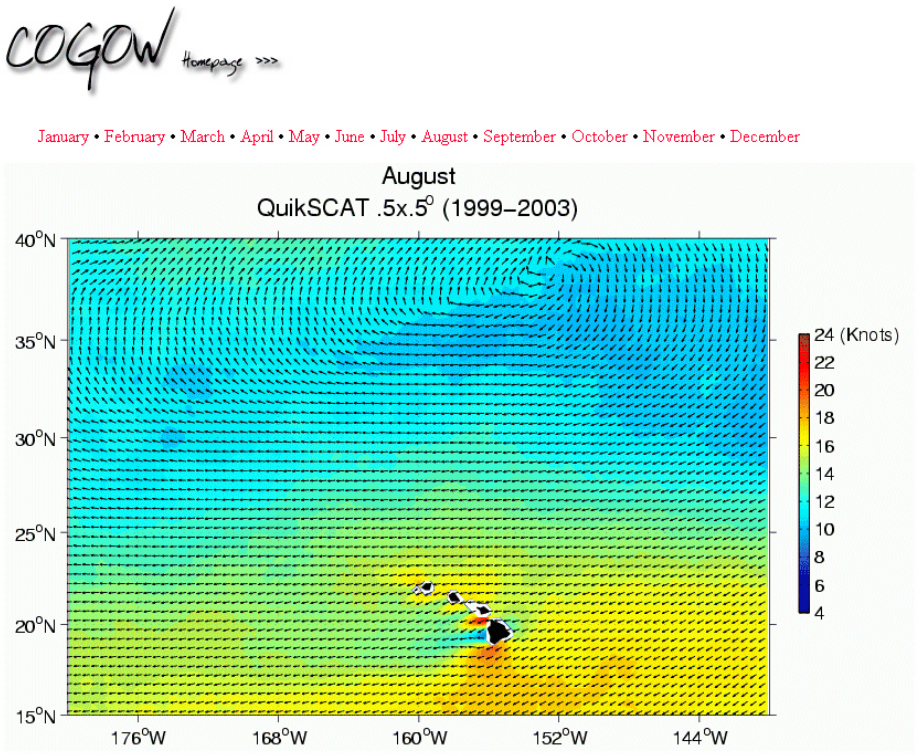

Figure 13. The same as Figure 12 except that the vector averaged climatological wind directions are plotted on a 0.5° x 0.5° grid.

Running the cursor over this sub-regional map produces a wind rose plot to the right of the map that changes as the position of the cursor changes. A description and interpretation of these wind rose plots was given previously in the discussion of Figure 5.

Placing the cursor on the wind vector situated directly south of the Island of Oahu (21.75°N 157.75°W) produces the map and wind rose plot shown in Figure 14.

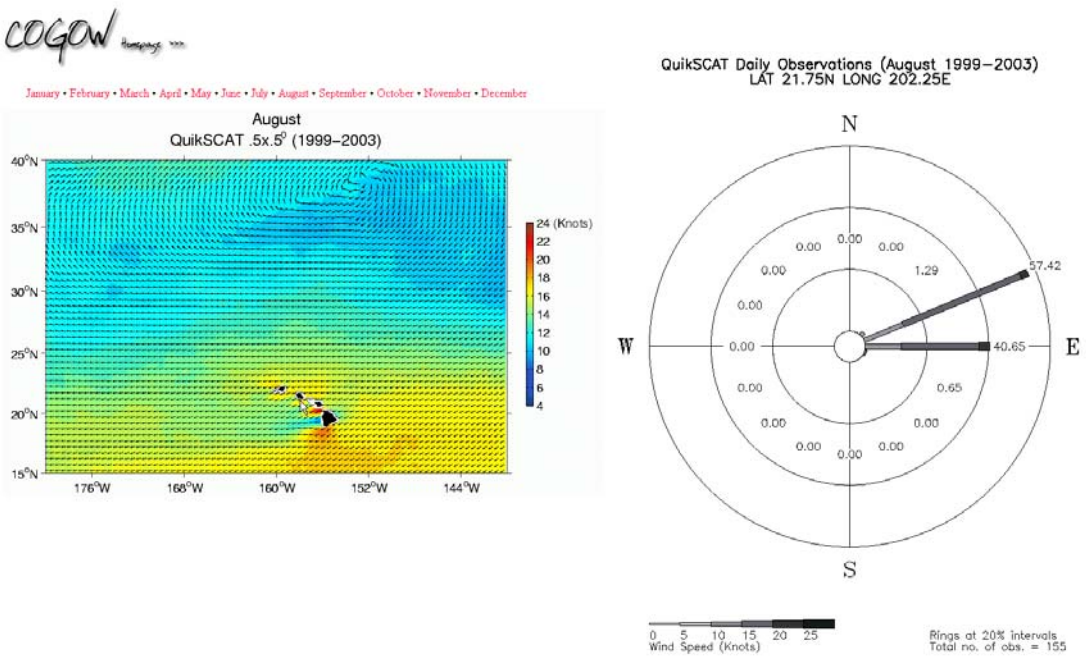

Figure 14. A screenshot from COGOW that shows an August sub-regional map (left panel) and a wind rose plot (right panel) that summarizes the statistics of the winds within the 0.5° x 0.5° grid cell centered at 21.75°N 157.75°W.

A blowup of the August wind rose plot for this location is shown in Figure 15. For the month of August (1999-2003) at 21.75°N 157.75°W, the winds tend to blow from the east and east-northeast for 40.7 % and 57.4 % of the time respectively. The east-northeasterly winds blow between 10 and 15 knots 13.6 % of the time, between 15 and 20 knots 41.3 % of the time and in excess of 20 knots 2.6 % of the time. The easterly winds blow between 10 and 15 knots 11.6 % of the time, between 15 and 20 knots 25.2 % of the time and in excess of 20 knots 3.9 % of the time.

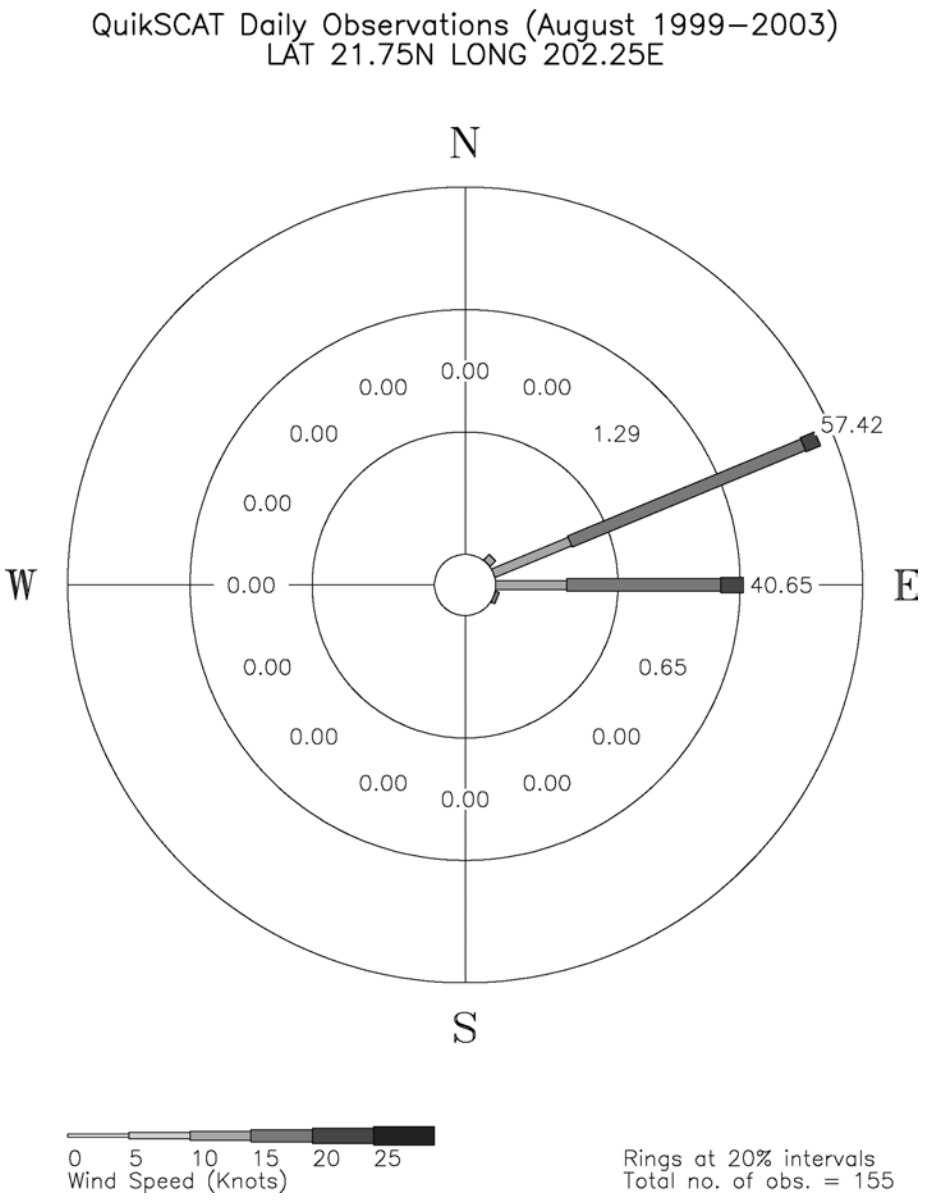

Figure 15. A wind rose plot that summarizes the August (1999-2003) winds within the 0.5° x 0.5° grid cell centered at 21.75°N 157.75°W.

Without moving the cursor, left-click on the wind vector situated directly south of the Island of Oahu to produce the popup box shown in Figure 16. Internet Explorer users please note that if this does not work it may be because your Internet Explorer popup blocker is activated. This can be overcome by either holding down the "Ctrl" key while left-clicking or you can left-click on the "Tools" dropdown menu located at the top of the Internet Explorer screen. Left-click on "Internet Options…" A popup box with a number of tabs should appear on the screen. These tabs include a "General" tab, a "Security" tab and a "Privacy" tab. Left-click on the "Privacy" tab. If the box labeled "Block pop-ups" is checked, uncheck it by left-clicking on the box. Left-click the "OK" button.

Again, place the cursor on the wind vector situated directly south of the Island of Oahu (21.75°N 157.75°W). Without moving the cursor, left-click on this wind vector to produce the popup box shown in Figure 16.

Figure 16. An example of the popup box that allows users to save a wind rose of interest in a graphical, tabular or raw format.

This popup box allows the user to save a wind rose of interest in either graphical (e.g., Figure 15), tabular (e.g., Table 2) or raw data form (e.g., Appendix B).

To save the wind rose plot to your local computer, right-click on the link entitled, "Graphical form of the wind rose plot". Left-click the "Save Link As…" option. Then save the image file to the desired folder or directory.

To save the tabular and raw data versions of the wind rose plot, repeat the above steps for the links entitled, "Tabular form of the wind rose plot" and "Wind speed and direction data used to create the wind rose plot" respectively.

To close the popup box, left-click "Close Window".

Using the Climatology of Global Ocean Winds, we are now in a position to better answer the two questions proposed for the NOAA OR&R analysis of possible oil spill trajectories in the proposed August recovery of *Ehime Maru*:

1. How representative is the assumed wind speed of 10 knots?
2. How variable is the wind field off the island of Oahu in terms of wind direction for the month of August?

The answer to the first question is that NOAA OR&R's usage of a 10 knot wind in their modeling effort significantly underestimated average wind speeds within this region. COGOW shows that average wind speeds are more typically between 15 and 20 knots. Note that, if anything, this value of between 15 and 20 knots may be biased somewhat low as it is derived from data that are temporally averaged to 3-day composites.

With regard to the second question, the user will recall that NOAA OR&R's model results (Figures 6 and 7) showed that easterly winds would result in diesel fuel being pushed toward the beach at Barbers Point during both ebb and flood tide conditions. East-northeast winds could potentially result in diesel fuel being pushed toward the beach during both ebb and flood tidal conditions; however, it appeared to be much more likely during flood conditions. North and northeast wind would result in the plume being pushed offshore after 24 hours in all conditions. Figure 15 shows there to be low variability of wind direction at this location during August. Over 98 % of the time, the winds blow from either the east-northeast or east. It therefore appears from NOAA OR&R's model results that, if the fuel tanks of *Ehime Maru* had in fact ruptured during the recovery operation, oil spill responders may have been somewhat unprepared for the resulting spill.

Chapter 4: Examples of Phenomena Observed Within COGOW

The following examples of phenomena (the south Asian monsoon, sea surface temperature (SST) and wind field coupling, gap winds and corner accelerations) that are visible within COGOW are intended to provide starting points for the reader's exploration of this climatology. These four sections should be read in conjunction with COGOW's online content[5].

While aspects of the phenomena discussed here, such as the interannual variability of in south Asian monsoon winds or the volume transport of the Agulhas Current, are not visible within COGOW, these discussions are included to place these phenomena in a physical/cultural context. In addition, it is hoped that these discussions will pique the reader's interest with respect a particular phenomenon or aspect of that phenomenon thereby enticing the reader to conduct further personal research.

The South Asian Monsoon

Introduction

The word "monsoon" is thought to have originated from the Arabic word *mausim* meaning season. The distinguishing characteristic of the monsoonal regions of the world is the seasonal reversal in wind direction (Ramage, 1971). These reversals have led the inhabitants of regions such south Asia, in particular India, to divide their lives, customs and economies into two distinct phases: the "wet" and the "dry". The wet phase refers to the summer monsoon (or the so-called southwest monsoon, named after the direction of the prevailing surface wind). For most of India, the summer monsoon extends from June through September. The dry phase refers to the winter monsoon, or northeast monsoon, which extends from December through February.

[5] http://www.cioss.coas.oregonstate.edu/cogow

The precipitation patterns associated with these two phases of the monsoon are shown in Figure 17.

The south Asian monsoon exists with considerable temporal and spatial variability. Arguably the three most important features of intraseasonal variation is the timing of the onset of the summer monsoon (Webster *et al*., 1998), the fluctuation between active and weak periods (Gadgil and Josef, 2003), and the northward propagations of the tropical convergence zone (TCZ) at intervals of 2-6 weeks throughout the summer monsoon (Annamalai and Slingo, 2001). Rainfall associated with the south Asian monsoon also exhibits interannual variability on timescales of between three and seven years. While this mechanism is not fully understood, Webster *et al*. (1998) show the All-India Rainfall Index (AIRI) to be associated with the El Niño Southern Oscillation (ENSO) phenomenon (Rasmusson and Carpenter, 1982) at interannual timescales. This relationship is shown qualitatively in Figure 18, which shows that rainfall tends to be stronger during La Niña years and weaker during El Niño years.

The agricultural practices of countries such as India are intricately connected to the monsoon cycle. While the regularity of the warm moist and cool dry phases of the monsoon appears ideal for agrarian societies, agriculture is extremely susceptible to minor changes in the annual cycle. Small variations in the timing and/or quantity of rainfall, for example a late versus early onset of the monsoon, an ill-timed lull in monsoon rainfall, or a year of below-normal rainfall, can result in significant societal impacts (Gadgil, 1996).

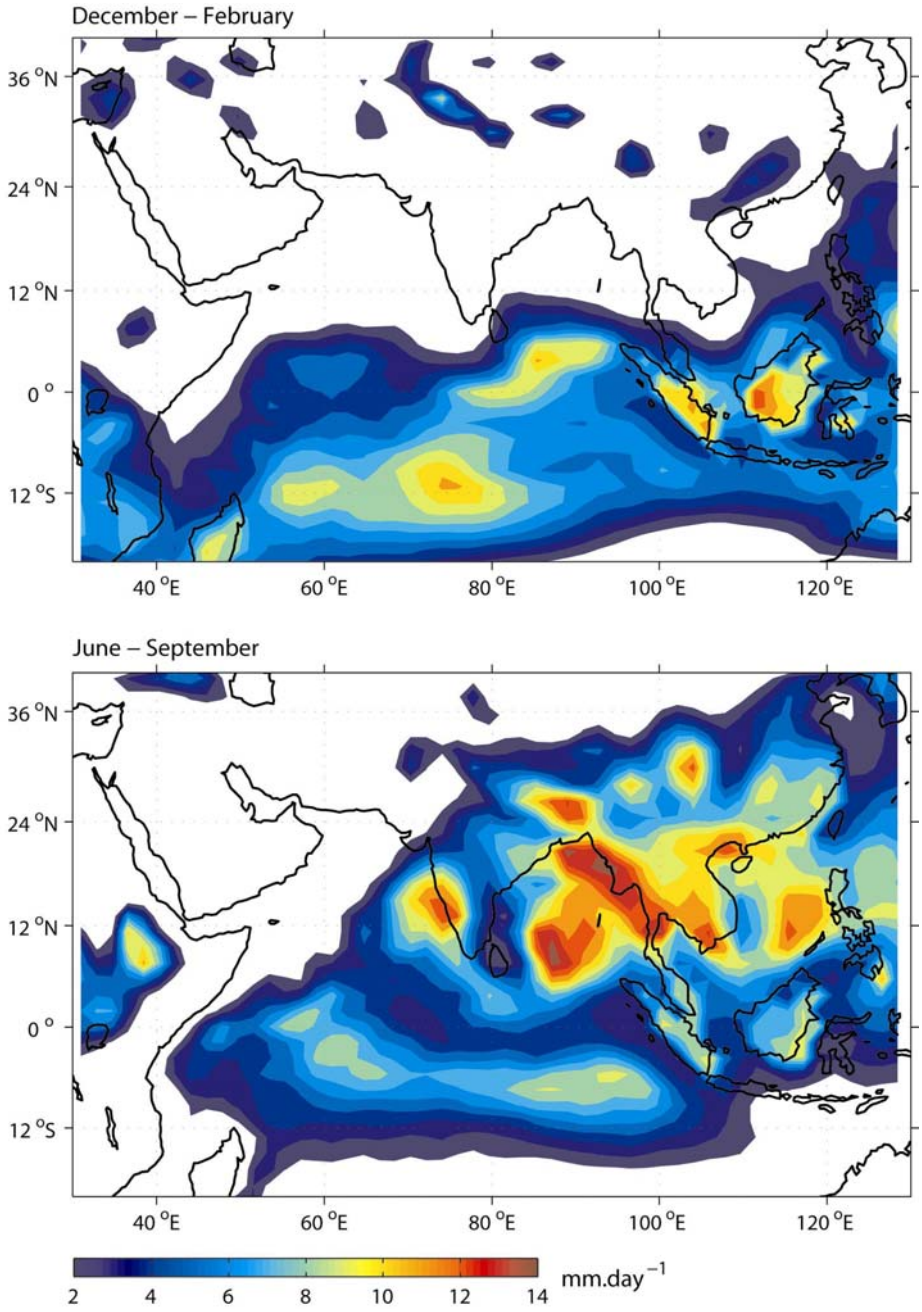

Figure 17. Long-term (1968-1996) daily surface precipitation rate composites derived from the 1.875° x 1.875° resolution NCEP/NCAR reanalysis fields (Kalnay *et al*., 1996) for the northeast (top panel) and southwest (bottom panel) monsoons. Note that these plots depict the seasonal mean rainfall rates. Monsoon rainfall does not occur as a continuous deluge but is punctuated by considerable variability within any particular season.

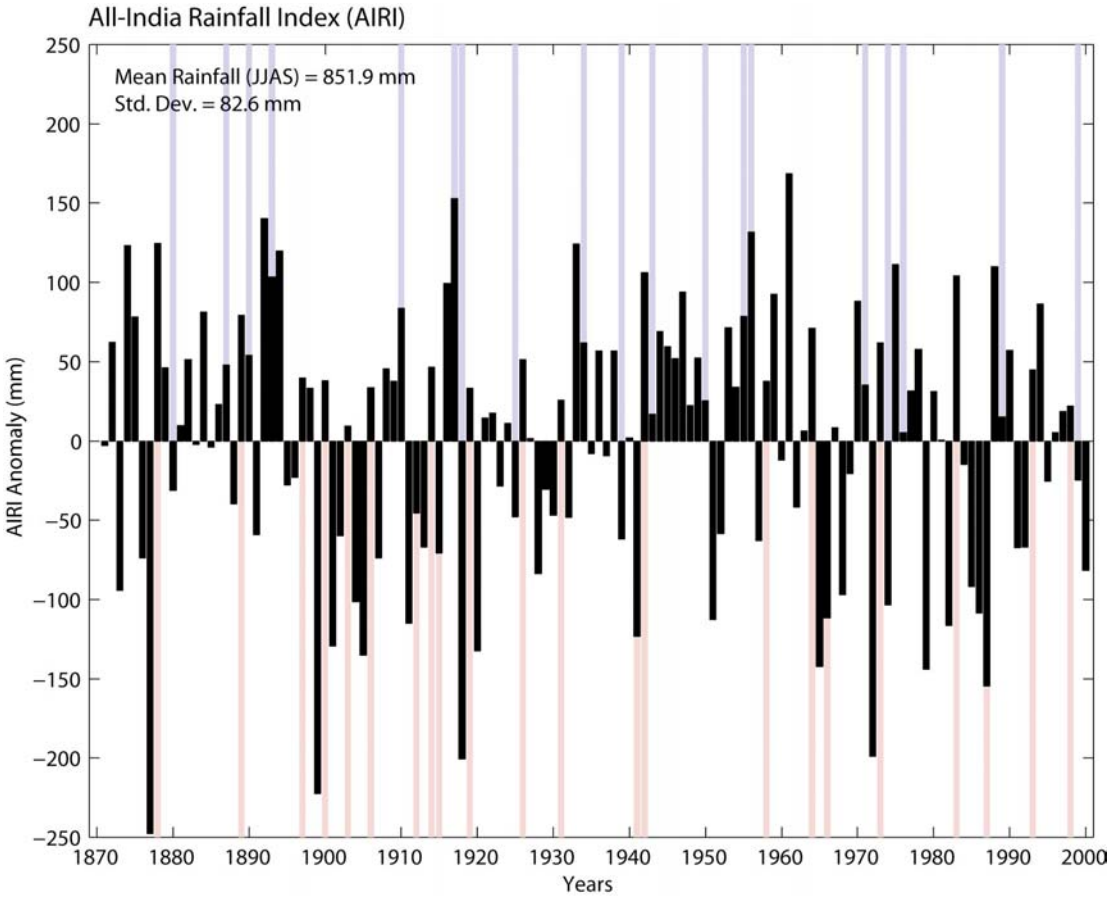

Figure 18. The All-India Rainfall Index for June through September (1871-2000) (Parthasarathy *et al*., 1995). The light red and blue lines indicate El Niño and La Niña events respectively (Reason *et al*., 2000).

The Basic Mechanism

The original model by Halley (1686) explained south Asian monsoon dynamics based on the differential heating of land and sea. In this conceptual model, the land warms to a temperature higher than that of surrounding oceans during summer months. The ascending warm air causes an onshore movement of relatively cool moist oceanic air, bringing the rains associated with the monsoon. Cooling over the continent during winter sees the reverse occurring, i.e., the offshore flow of air and dry conditions over the land. Simpson (1921) shows that the observations of the space-time variations of the monsoon over India are not consistent with Halley's (1686) hypothesis. He points

out that India is much hotter in May, before the onset of the monsoon, than in July, when the monsoon is at its height. In addition, Simpson (1921) draws attention to the fact that the hottest part of India, the northwest, gets little to no rain during the summer monsoon. He therefore suggests that the summer monsoon is the result of a combination of factors including, temperature, pressure, humidity, the Coriolis effect, and the geographical distribution of mountain ranges.

A number of authors have proposed a hypothesis in which the monsoon is considered to result from the seasonal migration of the TCZ (Gadgil, 2003) or the equatorial trough (Riehl, 1979) in response to seasonal variations in the latitude of maximum insolation and the differential heating of air over the Tibetan High Plateau (Yanai *et al*., 1992). Gadgil (2003) provides a comprehensive review of a number of studies that, using satellite and conventional observations, support this hypothesis.

The seasonal reversals in surface wind direction are clearly visible within COGOW (Figures 19 and 20). These figures show the monthly evolution of surface winds over the Arabian Sea and the Bay of Bengal. During the Boreal winter (December, January and February), the monsoon winds are directed away from the Asia, resulting in northeast winds over the Arabian Sea and the Bay of Bengal. In contrast, southwesterly monsoon winds are observed over both basins during the months of late spring and summer (May, June, July, August and September). The southwesterly winds over the Arabian Sea are a continuation of the southern-hemisphere trade winds. Associated with the onset of these southwesterly surface winds is the spin-up of the Somali Current, the western boundary current for the northern Indian Ocean (Schott and McCreary, 2001). Characteristic features of the Somali Current are two large anticyclonic eddies, the so-called “Great Whirl” (Schott *et al*., 1997) and the so-called “Southern Gyre” (Schott and McCreary, 2001). These eddies are bordered along the coastal margin of Somalia by zones of strong upwelling (Figure 21) that exhibit significant summertime chlorophyll-*a* maxima (Baars *et al*., 1998).

At higher altitudes the southwesterly cross-equatorial winds develop into a low level jet (LLJ). This LLJ, sometimes referred to as the so-called “Findlater Jet”, develops close to the east African coast and has a core at approximately 850 hPa (Findlater, 1969). From monthly mean wind data, Findlater (1971) suggests that this LLJ splits into two eastward flowing braches east of 60°E. The southern branch is said to be located to the south of India (8°N) while the northern branch is located at about 17°N. In a recent study using NCEP-NCAR reanalysis fields, Joseph and Sijikumar (2004) were unable to find support for the splitting of the LLJ over the Arabian Sea suggested by Findlater (1971). These authors demonstrate that the position of the LLJ is associated with active and weak monsoon periods. During active periods there is no splitting of the LLJ over the Arabian Sea. The core of this single axis jet is located at about 15°N. Two branches of the LLJ are, however, observed during weak monsoon periods. During these periods, one branch passes eastward close to Sri Lanka at about 8°N while a second branch is located at about 25°N, rather than at 17°N as suggested by Findlater (Joseph and Sijikumar, 2004).

A possible surface expression of the LLJ is observable in the July (2000-2004) (Figure 20) large-scale wind speed maxima located off the Somali coast and over the Arabian Sea, as well as to the south of India and Sri Lanka.

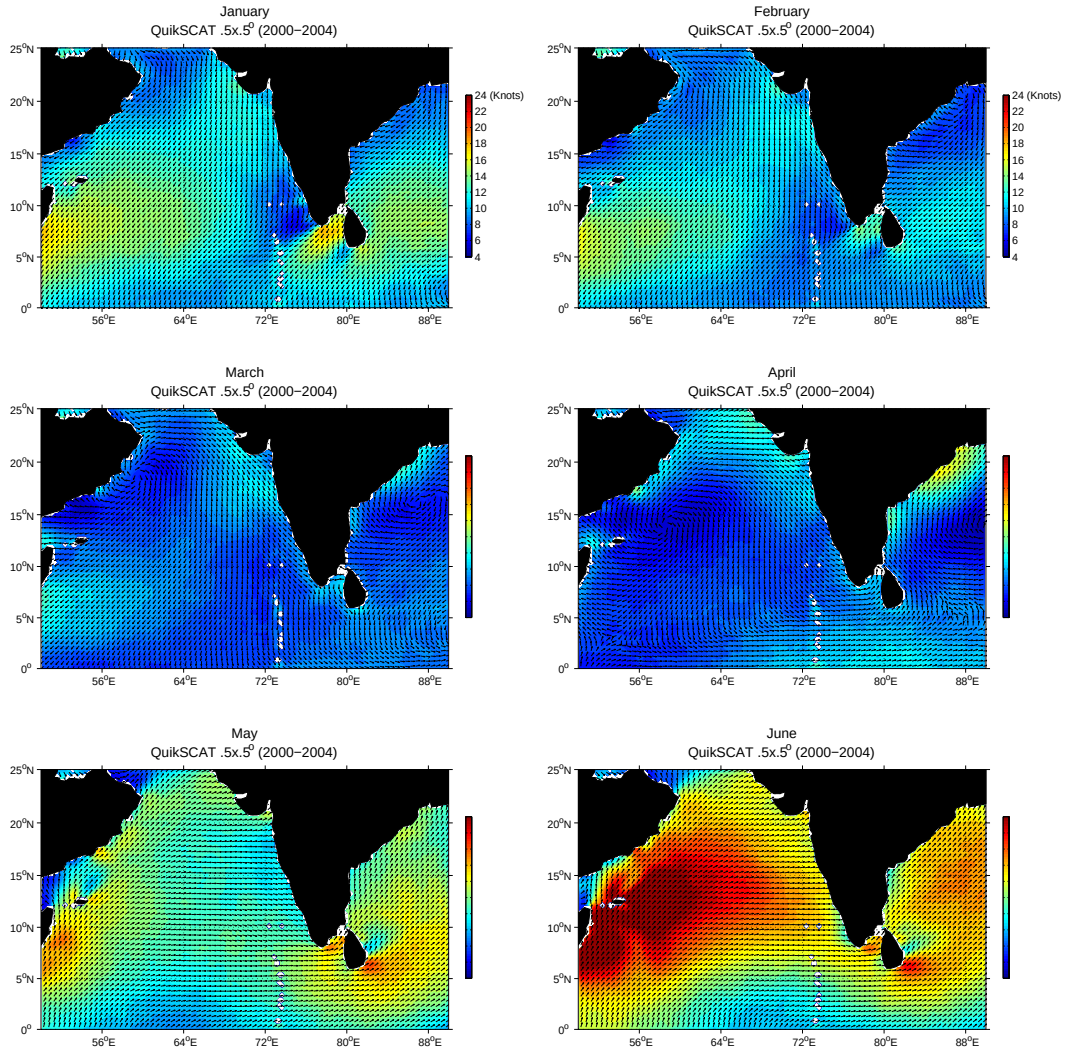

Figure 19. Composite averages of the wind field at 10 m derived from the QuikSCAT scatterometer for the month of January (top-left panel) through to June (bottom-right panel). Scalar averaged wind speed is shown in color on a 0.25° x 0.25° grid. Vector averaged climatological wind directions are plotted as unit vectors on a 0.5° x 0.5° grid. Note the northeasterly winds over the Arabian Sea and the Bay of Bengal during the winter months of January and February. In contrast, the months May and June show southwesterly winds over both basins.

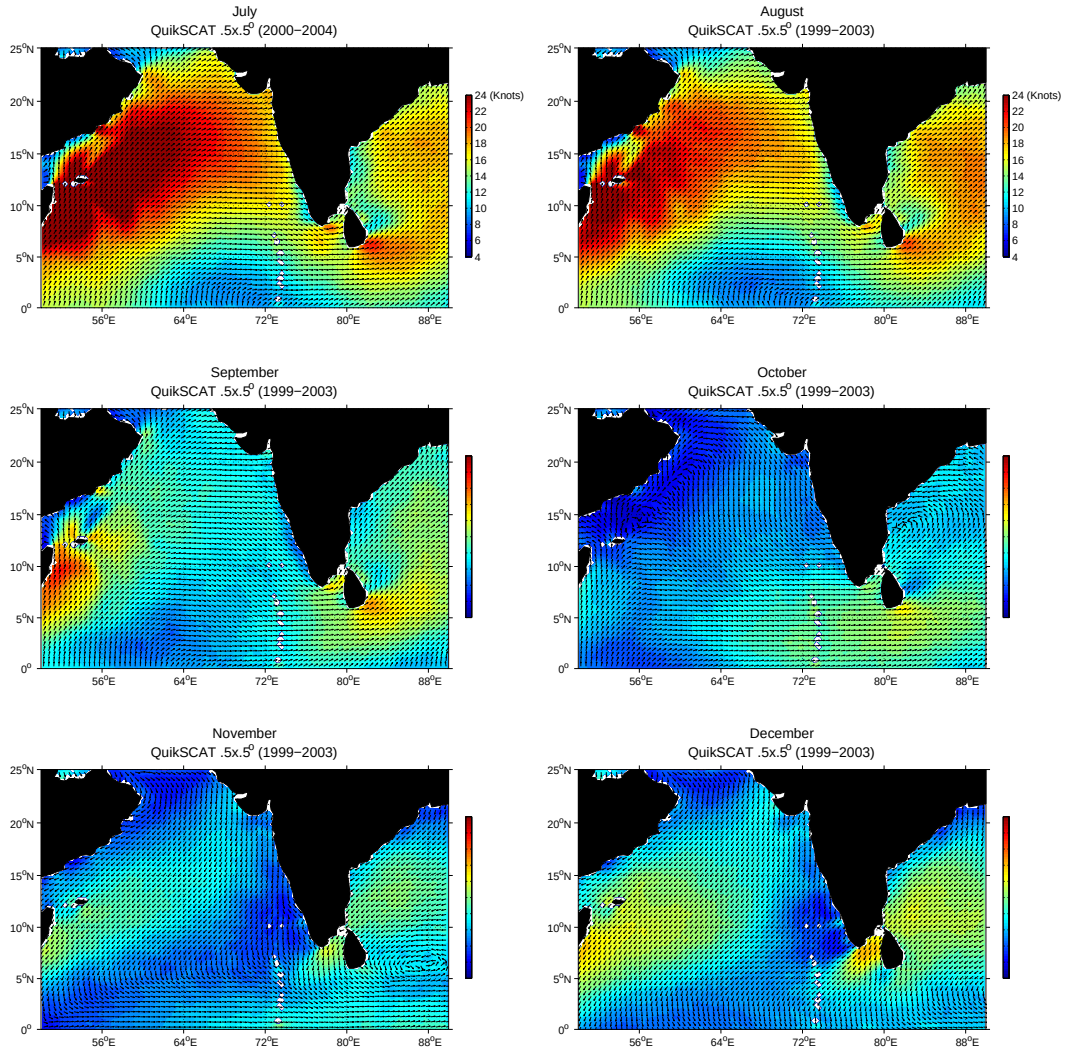

Figure 20. The same as Figure 19 expect for the monthly composite for July (top-left panel) through to December (bottom-right panel). Note the southwesterly winds over the Arabian Sea and the Bay of Bengal during the summer months of July, August and September. In contrast, the months November and December show northeasterly winds over both basins.

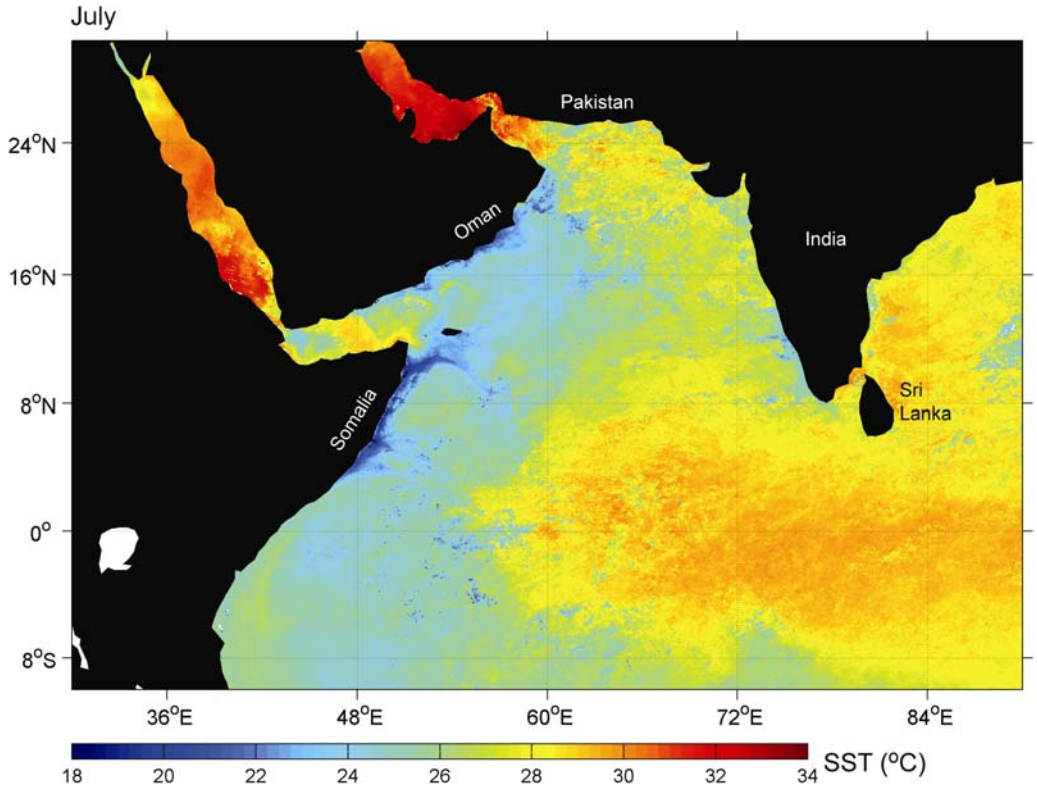

Figure 21. MODIS (11 and 12 µm) monthly SST composite for July 2003. July is the height of the southwest monsoon. During this period both the Great Whirl and the Southern Gyre are well established. This circulation pattern is revealed in the coastal upwelling off the coast of Somalia. These data are plotted on a 4 km square grid.

Evidence of SST and Wind Field Coupling in the Southwest Indian Ocean

Introduction and Background

The Agulhas Current that flows poleward near the western boundary of the southwest Indian Ocean was first documented toward the end of the fifteenth century by Portuguese mariners, such as Vasco da Gama, seeking a trade route to India (Pearce, 1980). Within a century of its discovery, the strength and general location of this boundary current and other components of the Agulhas Current system were sufficiently known that ships would take advantage of it when sailing westward but would sail to the south of it into the region of the Agulhas Return Current when sailing eastward (Pearce, 1980).

The Agulhas Current, the largest western boundary current in the world ocean with an average volume transport of 69.7 ± 4.3 Sv[6] (Bryden *et al*., 2005) forms part of the southwest Indian Ocean subgyre (Stramma and Lutjeharms, 1997). This fast flowing (> 2 $m.s^{-1}$) (Boebel *et al*., 1998) current closely follows the continental shelf break of southeast Africa from 27° to 40°S (Gründlingh, 1983) (Figures 22 and 23).

[6] 1 Sv = 1 x 10^6 $m^3.s^{-1}$

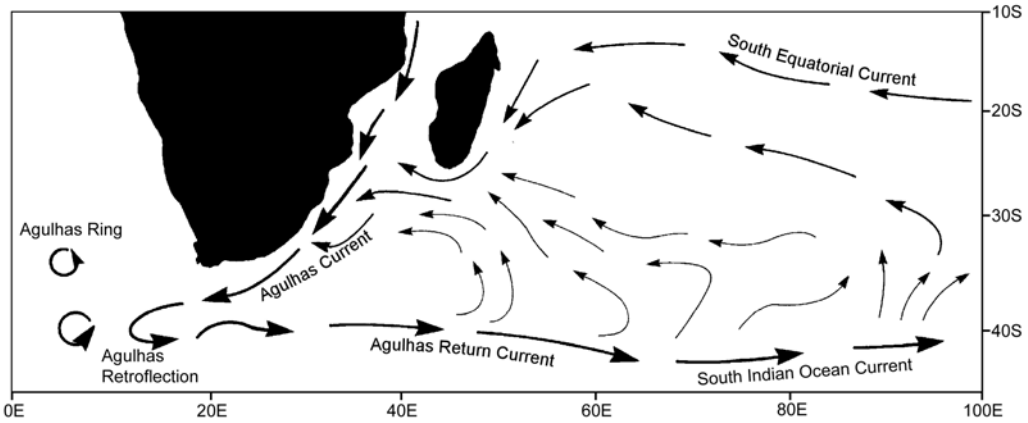

Figure 22. A schematic of the Agulhas Current system (modified from Lutjeharms and Ansorge, 2001).

As the Agulhas Current reaches the southern tip of the continental shelf, known as the Agulhas Bank (Figure 23), the southwestward flowing current retroflects, or turns back on itself. This region is known as the Agulhas Retroflection (Bang, 1970) (Figure 22).

After the Agulhas Retroflection, the flow becomes known as the Agulhas Return Current (ARC) (Figure 22). This current flows eastward with a quasi-stationary meandering pattern between 38° and 40°S and surface velocities of up to 2.1 $m.s^{-1}$ (Boebel *et al*., 2003). The ARC is associated with a strong temperature front. In keeping with Lutjeharms and Valentine (1984) this temperature front will hereafter be referred to as the Agulhas Front (AF). Space-time composites (Belkin and Gordon, 1996) reveal the remarkably stable positions of two meanders within the AF located to the east of the Agulhas Retroflection. The first meander coincides with the location of the Agulhas Plateau (Figure 23), a major bathymetric obstacle that lies across the path of the ARC. This meander is evident in Figure 24 as a relatively cold northward intrusion of surface waters located at about 38°S 26°E. The second meander is located farther downstream, at about 33°E. Studies by Weeks *et al*. (1998) and Boebel *et al*. (2003) confirm the stability of these two meanders. These authors find

the first meander to be located, on average, at 26.9°E, while the second meander is located, on average, at 32.8°E.

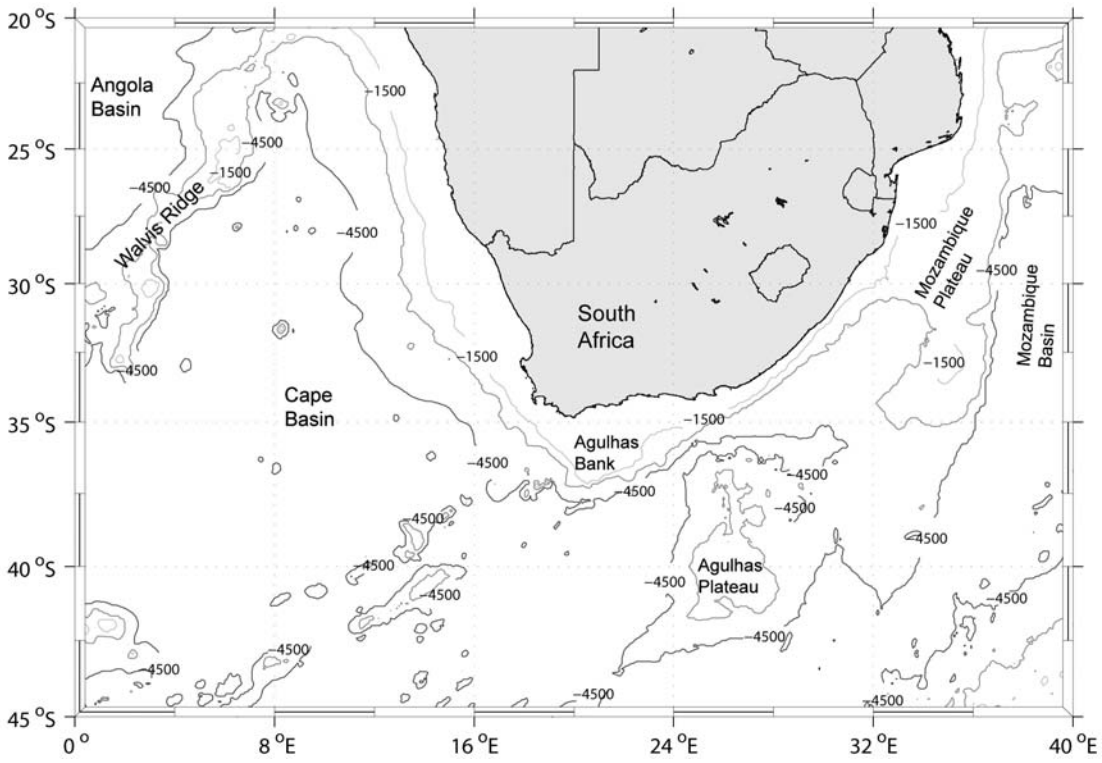

Figure 23. Bathymetry of the southeast Atlantic and southwest Indian Oceans. Note the Agulhas Plateau to the southeast of the Agulhas Bank. This major bathymetric feature is thought to play a significant role in the positional stability of the first meander of the ARC (Boebel *et al*., 2003). The contour interval is 1500 m.

Coupling of Surface Winds and the Agulhas Current System

The Agulhas Current system is subject to strong SST gradients. Annually averaged SST gradients across the ARC can exceed 4°C $(100\ km)^{-1}$ (O'Neill *et al*., 2005). As reviewed by O'Neill *et al*. (2003; 2005), Xie (2004) and Chelton *et al*. (2004), strong ocean-atmosphere interactions are evident in such regions of strong SST gradients from satellite observations, as well as from analytical and mesoscale atmospheric models as suggested by Sweet *et al*. (1981), Jury and Walker (1988) and

Wallace *et al*. (1989). SST gradients influence the marine atmospheric boundary layer (MABL) by modifying its stability through changes in air-sea heat flux. Lindzen and Nigam (1987), Small *et al*. (2005) and Samelson *et al*. (2005) argue that SST induced pressure gradients and boundary layer thickness also play important roles in the wind response to SST. Colder waters act to stabilize the MABL. This inhibits the vertical turbulent mixing of momentum from aloft to the surface and results in a shallowing of the MABL and a deceleration of surface winds. This deceleration in surface wind speeds over cold water is observable within COGOW (Figure 25). Figure 25 shows local minima in QuikSCAT wind speeds located at about 38.5°S 26.5°E and 39.5°S 32.5°E for the months June through August. Note that these two locations coincide with the locations of the two meanders discussed above.

The reverse is true of warmer waters where increased surface heat fluxes destabilize and deepen the MABL. This destabilization enhances the vertical turbulent mixing of momentum from aloft to the surface and results in an acceleration of surface winds. COGOW shows this acceleration of surface winds as a ribbon-like feature stretching along the southeast coast of South Africa over the relatively warm Agulhas Current (Figures 22 and 24).

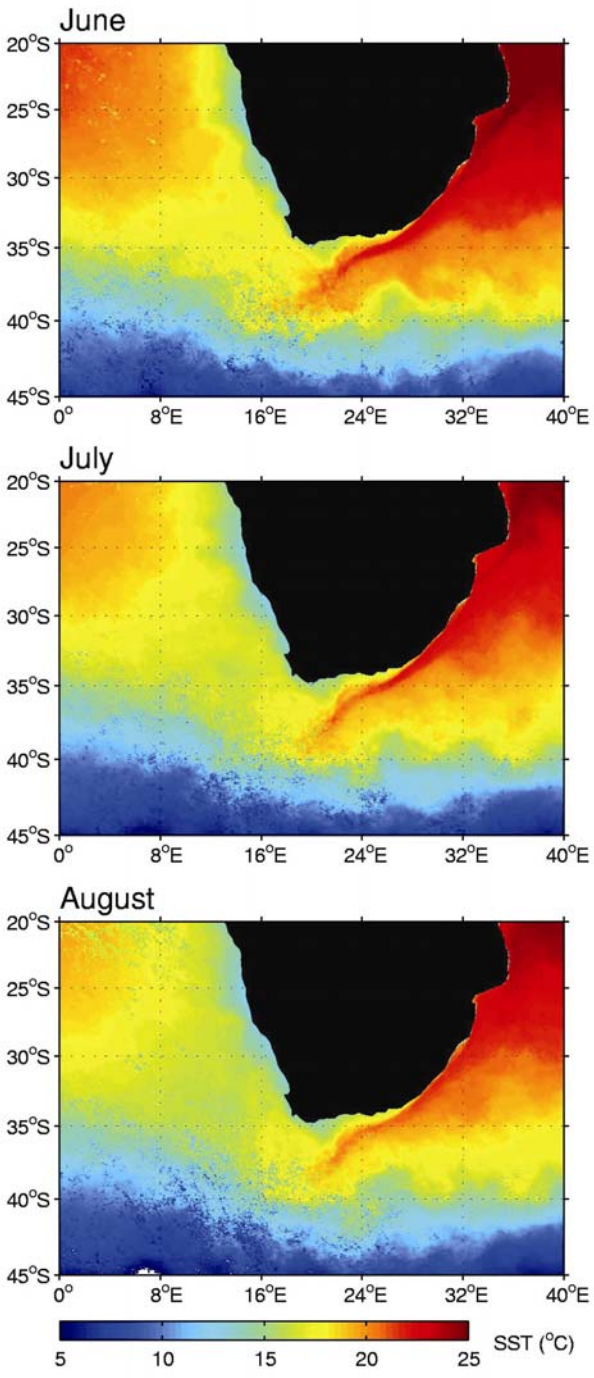

Figure 24. 5-year average MODIS (11 and 12 μm) monthly SST composites for June, July and August (2000-2004). These data are plotted on a 4 km square grid. Note the positions of the two ARC meanders located to the east of the Agulhas Retroflection at about 26 and 33°E respectively.

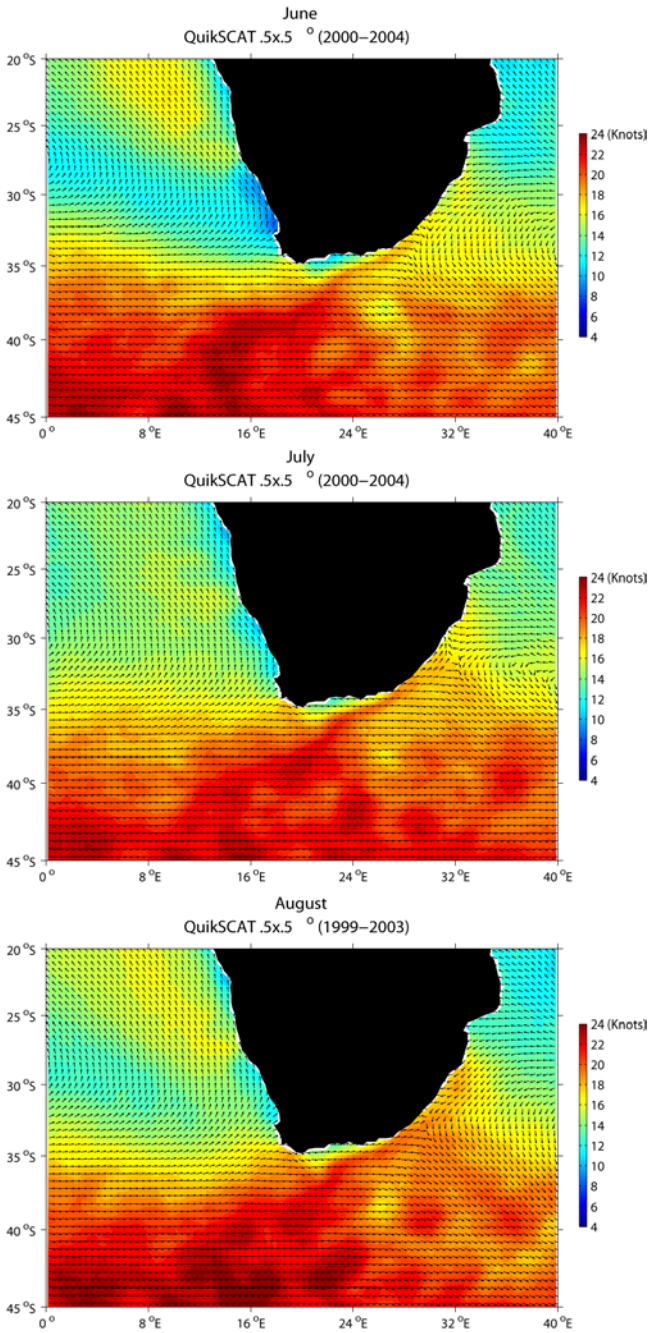

Figure 25. Composite averages of the wind field at 10 m derived from the QuikSCAT scatterometer for the month of June (Top) through to August (Bottom). Scalar averaged wind speed is shown in color on a 0.25° x 0.25° grid. Vector averaged climatological wind directions are plotted as unit vectors on a 0.5° x 0.5° grid. Note the region of reduced wind speeds at about 38.5°S 26.5°E and 39.5°S 32.5°E.

As shown in O'Neill *et al*. (2003; 2005), the acceleration and deceleration of surface winds in the ARC region results in short-scale changes in the wind stress curl fields. With regards to the meander situated over the Agulhas Plateau one would expect to find, especially during the austral winter, a localized region of negative wind stress curl along its northern boundary. According to Ekman theory (Stewart, 2005), this region of negative curl should be subject to an upper ocean divergence, which in turn would result in upward Ekman pumping and enhanced biological productivity. Work by Machu and Garçon (2001) shows moderate support for this hypothesis. Using SeaWiFS ocean color data, they find an enhancement of biological production and chlorophyll-*a*, in the region of the Agulhas Plateau during the austral winter (Figure 8 of Machu and Garçon, 2001).

Coupling of SST and Surface Winds in other Regions of the World Ocean

Evidence of similar coupling between SST and surface winds is visible elsewhere within COGOW.

Figure 26 shows the deceleration of the southeasterly trade winds as they blow across the equatorial Pacific cold tongue into the ITCZ located about 12° north of the equator (Chelton *et al*., 2001). Figures 27 and 28 show a 6-7 knot increase in the climatological average surface wind speed across the relatively warm Kuroshio Current (Nonaka and Xie, 2003) and Gulf Stream respectively. A 6-7 knot increase in climatological average wind speed across the Gulf Stream is about 50 % weaker than the modification of wind speeds that have been observed at synoptic timescales (Chelton *et al*., 2006). Using data derived from a QuikSCAT overpass on 16 February 2005, these authors show wind speeds of 10-14 $m.s^{-1}$ on the south side of the North Wall of the Gulf Stream, defined to be the 17.5°C SST isotherm, and 4-7 $m.s^{-1}$ wind speeds on the north side of the North Wall. This greater than 7 $m.s^{-1}$ transition from high to low wind speeds occurred in less than 50 km (Chelton *et al*., 2006). Such

short-scale variability in wind speed should be factored into, amongst other things, the search and rescue operations of the U.S. Coast guard and other international search and rescue organizations such as South Africa's National Sea Rescue Institute (NSRI).

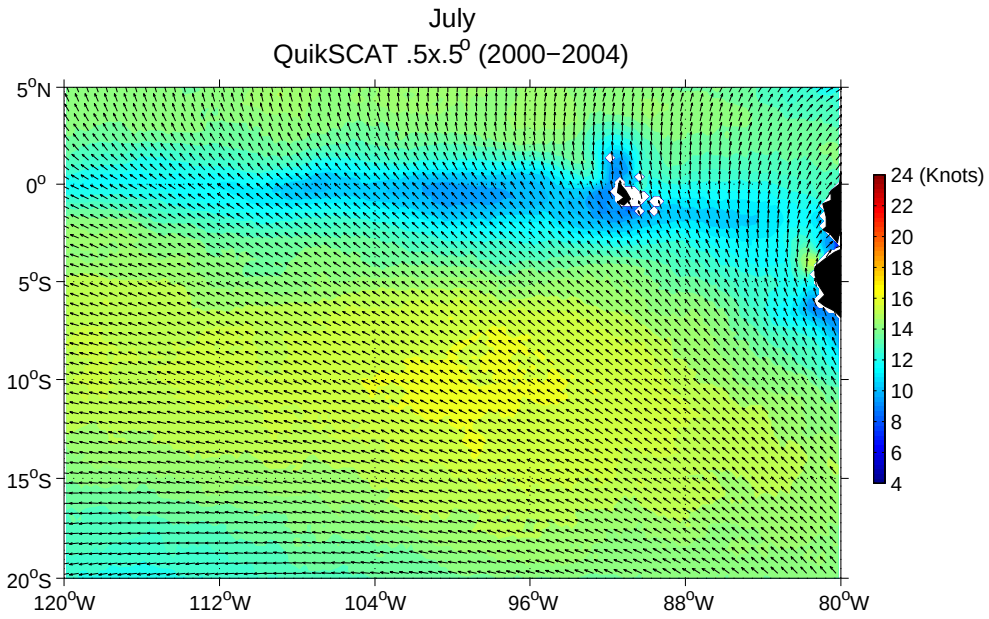

Figure 26. 5-year (2000-2004) monthly composite average of the wind field at 10 m derived from the QuikSCAT scatterometer for July. Scalar averaged wind speed is shown in color on a 0.25° x 0.25° grid. Vector averaged climatological wind directions are plotted as unit vectors on a 0.5° x 0.5° grid.

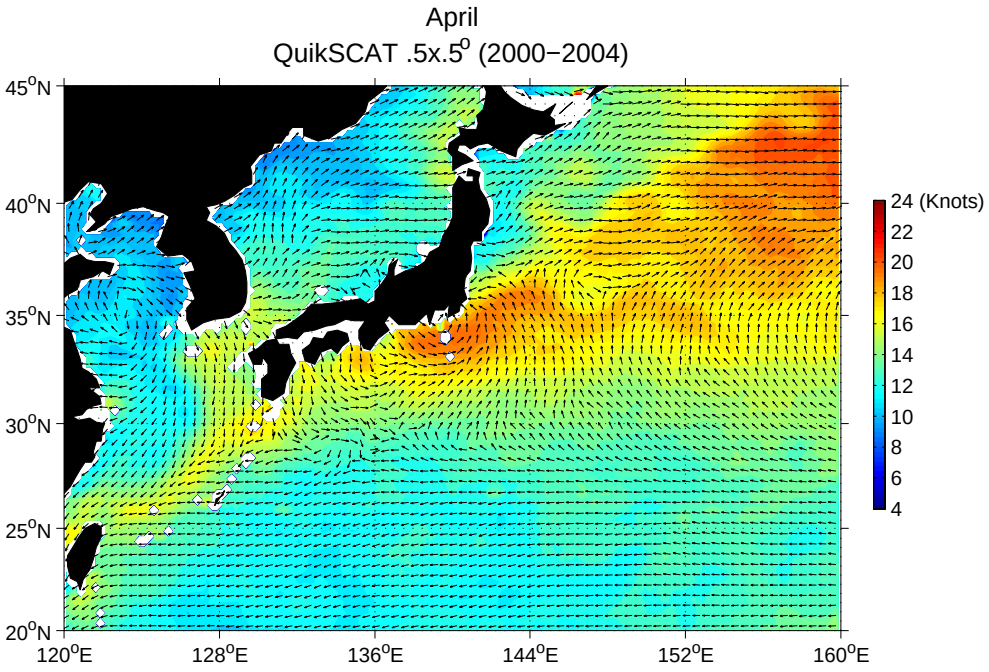

Figure 27. The same as Figure 26 expect for the monthly composite for April off the east coast of Asia.

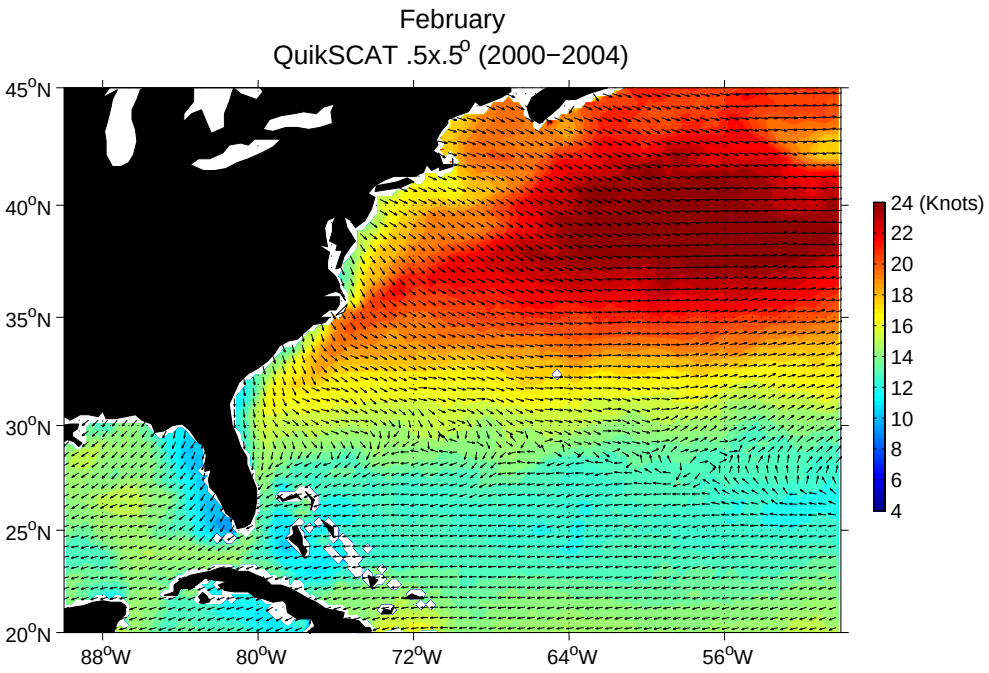

Figure 28. The same as Figure 26 expect for the monthly composite for February off the east coast of North America.

Gap Winds

Central America

With the onset of the boreal autumn, relatively high-pressure atmospheric systems begin to form over the Great Plains of North America and move southwards towards the Gulf of Mexico and the Caribbean Sea. Upon reaching the gulf the movement of these fronts is impeded to the west by the Sierra Madre. These mountains with an average elevation of over 1000 m form a natural barrier between the cold dense air masses to the east and the relatively warm low-pressure air over the eastern tropical Pacific. Three low-elevation passes through the mountains break this barrier. The 40 km wide Chivela Pass runs north to south from the Bay of Campeche to the Gulf of Tehuantepec (Figure 29). The other two passes are located in southern Nicaragua near the Gulf of Papagayo (Figure 29) and the Panama Canal (not shown).

In the vicinity of the Gulf of Tehuantepec, and at times the Gulf of Papagayo, large (> 5 hPa) sea level pressure (SLP) gradients drive strong winds through the passes and hundreds of kilometers into the eastern tropical Pacific (Chelton *et al*., 2000a). These winds can have sustained speeds of over 50 $m.s^{-1}$ (Stumpf, 1975) and therefore pose a significant threat to local mariners, especially those operating small fishing and sailing vessels. Upon leaving the Chivela Pass, the Tehuantepec gap winds, known locally as Tehuanos (Trasviña *et al*., 1995), initially follow an inertial trajectory turning in a clockwise direction (Bourassa *et al*., 1999) and eventually become easterly after geostrophic adjustment (Chelton *et al*., 2000b). At synoptic scales it was historically thought (Hurd, 1929) that these gap wind events were triggered sequentially from north-to-south (Schultz *et al*., 1997). Chelton *et al*. (2000a) demonstrate by means of three case studies that this is not necessarily the case. These authors' show that the Tehuanos and Papagayo gap wind events may occur either in sequence or independently.

Seasonal Variability

Using hourly wind data from the La Venta weather station located at the southern end of the Chivela Pass, Romero-Centeno *et al*. (2003) show this region to have an annual mean wind speed of 11 $m.s^{-1}$ with a standard deviation of 6.8 $m.s^{-1}$. These authors find the winds to be more intense during the winter with maxima in December and January. During this period, winds blow from a north-range (NNW through NNE) more than 75 % of the time. This intensity decreases towards summer reaching a minimum in May. A decrease in the frequency of north-range winds is also observed at this time. An interesting feature of this annual cycle is the relative maximum in north-range wind speed that is observed during July (Romero-Centeno *et al.*, 2003). Romero-Centeno *et al*. (2003) suggest that this relative maximum in wind speed occurs as a result of an increase in SLP in the Gulf of Mexico during July. This increase in SLP is caused by the westward displacement and intensification of the Bermuda High (Figure 30).

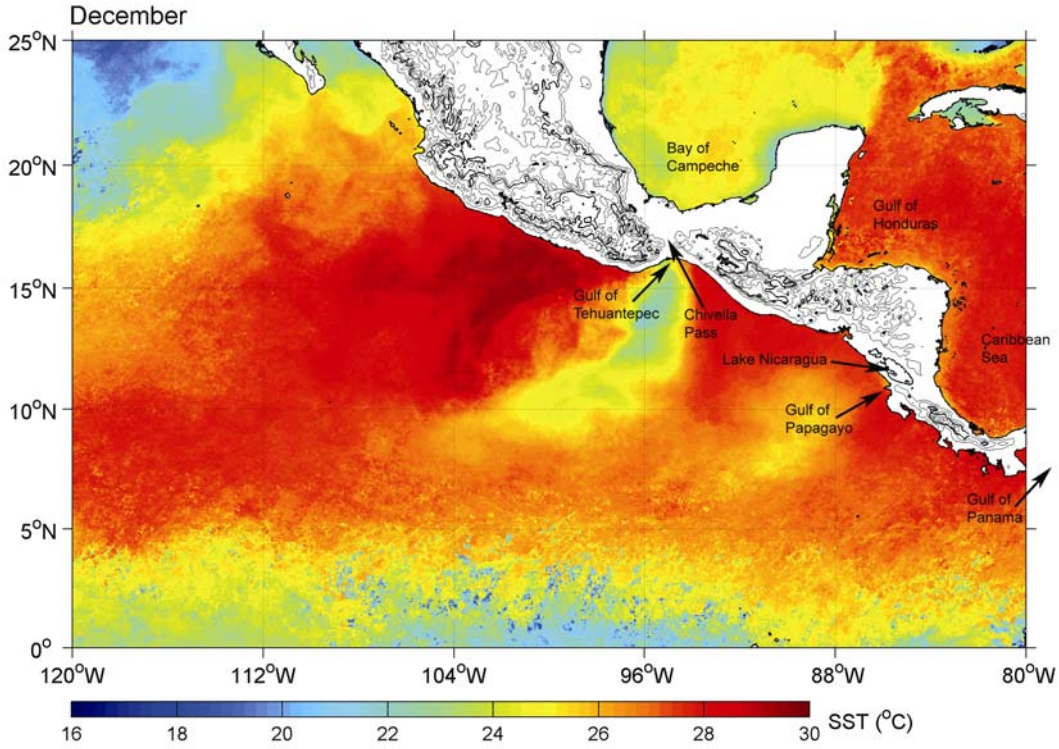

Figure 29. MODIS (11 and 12 µm) monthly SST composites for December 2003. These data are plotted on a 4 km square grid. The topography of southern Mexico and Central America is contoured with a 500 m interval. The 1500 m contour is shown in bold. Also shown are several of the geographic locations referred to in this section.

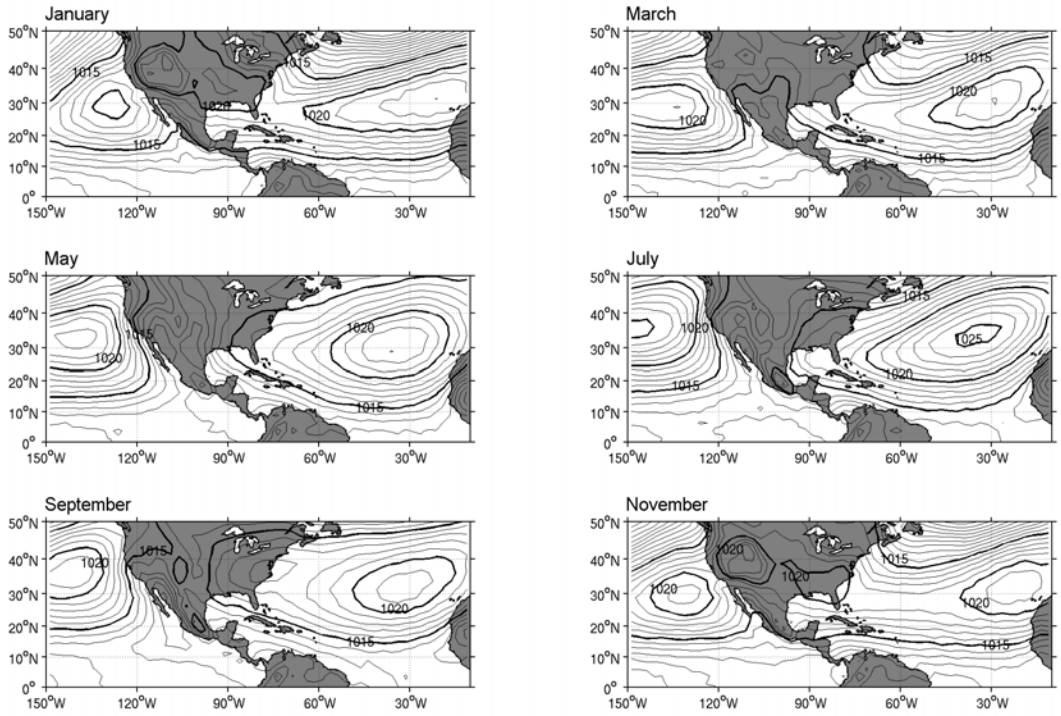

Figure 30. Long-term (1968-1996) monthly sea-level pressure composites derived from the 2.5° x 2.5° resolution NCEP/NCAR reanalysis fields (Kalnay *et al*., 1996). The contour interval is 1 hPa.

The Papagayo gap winds, or Papagayos (Schultz *et al*., 1997), are less variable both in term of speed and direction relative to the Tehuanos. The steadiness of these winds, which are for the most part an extension of the Caribbean trade winds, can be attributed to the underlying seasonal variation. This seasonal variation accounts for 54 % of the wind speed variance within the Gulf of Papagayo. In contrast, the seasonal variation of the Tehuanos accounts for only 16 % of the variance (Chelton *et al*., 2000a). During the 9-month time period September 1996 through June 1997, Chelton *et al*. (2000a) find the Papagayos to reach a maximum in late February 1997. This seasonal maximum coincides with the seasonal maximum of the Caribbean trade winds first noted by Chapel (1927) and shown in Figure 31.

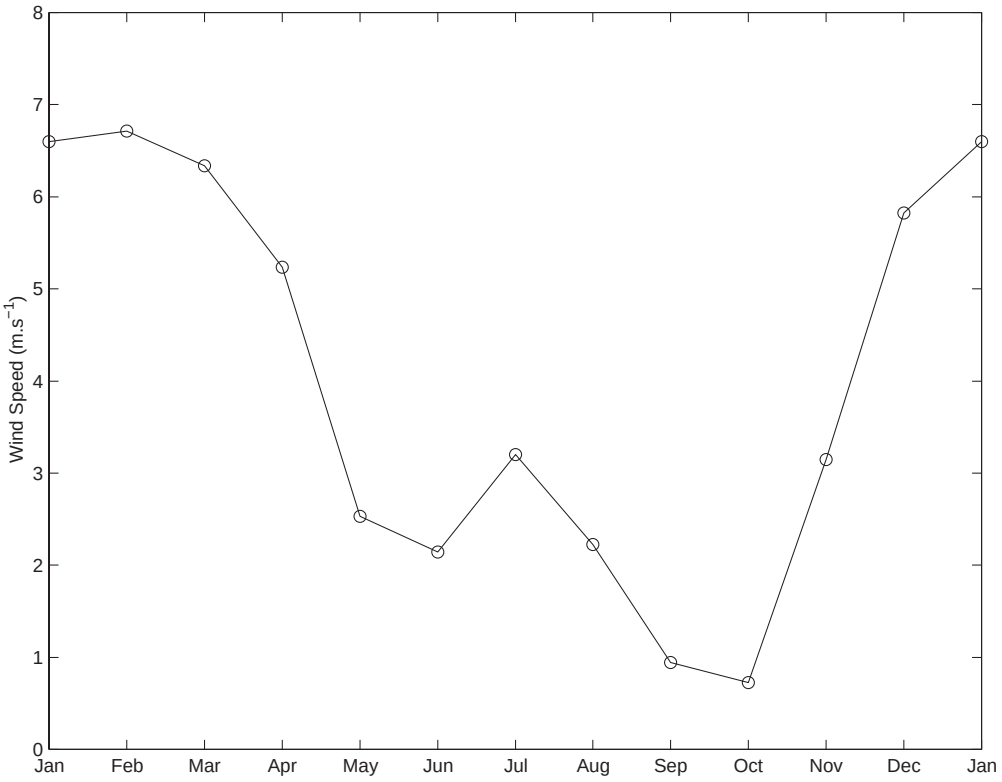

Figure 31. Long-term (1948-2004) monthly composite means of surface wind speed ($m.s^{-1}$) at 10°N 80°W derived from the 2.5° x 2.5° resolution NCEP/NCAR reanalysis fields (Kalnay *et al*., 1996).

The Tehuantepec and Papagayo gap wind events are shown by Chelton *et al*. (2000a) to occur at two and four-day timescales respectively. Because of the high frequency of occurrence of these events, they are clearly visible within COGOW's mean monthly composites of the surface wind field (Figures 32 and 33).

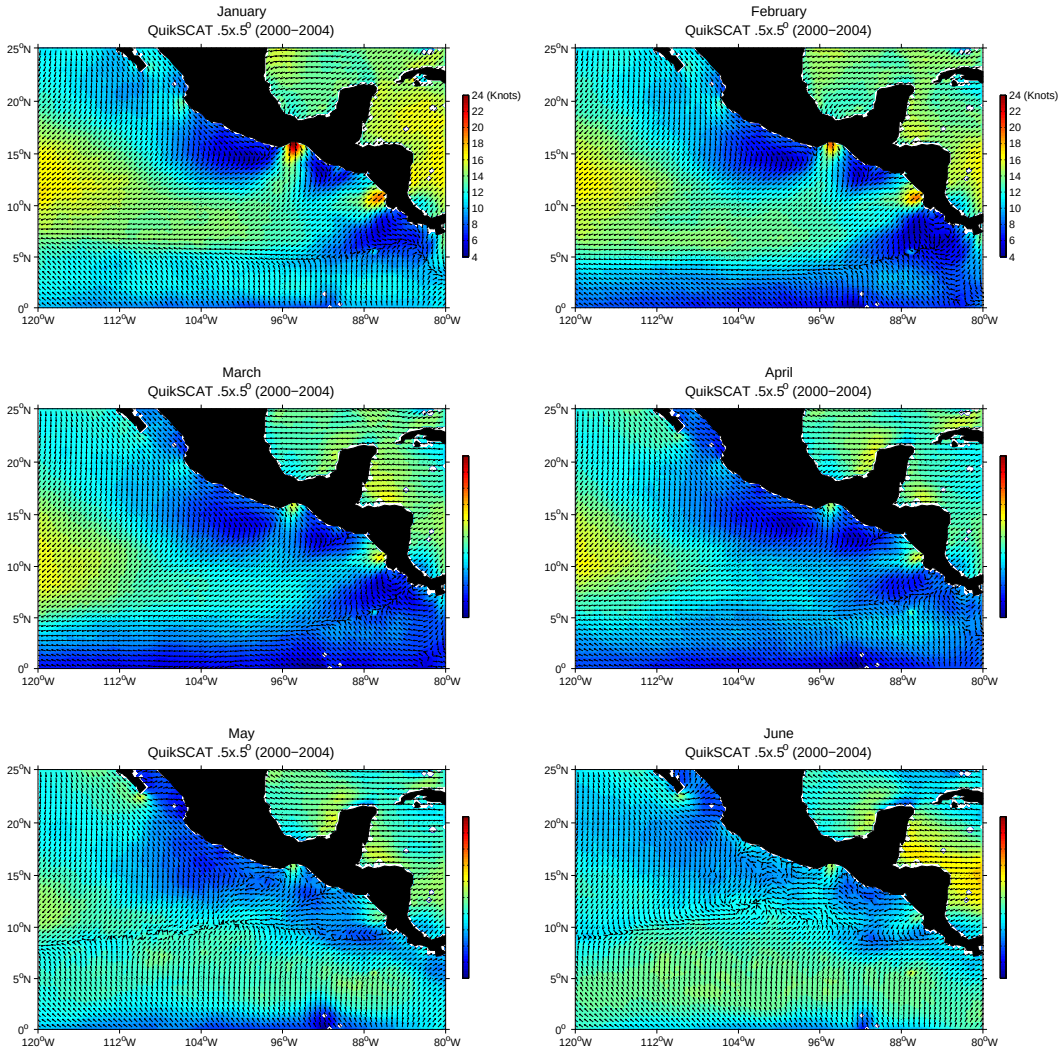

Figure 32. 5-year monthly composite averages of the wind field at 10 m derived from the QuikSCAT scatterometer for January (top-left panel) through to June (bottom-right panel). Scalar averaged wind speed is shown in color on a 0.25° x 0.25° grid. Vector averaged climatological wind directions are plotted as unit vectors on a 0.5° x 0.5° grid.

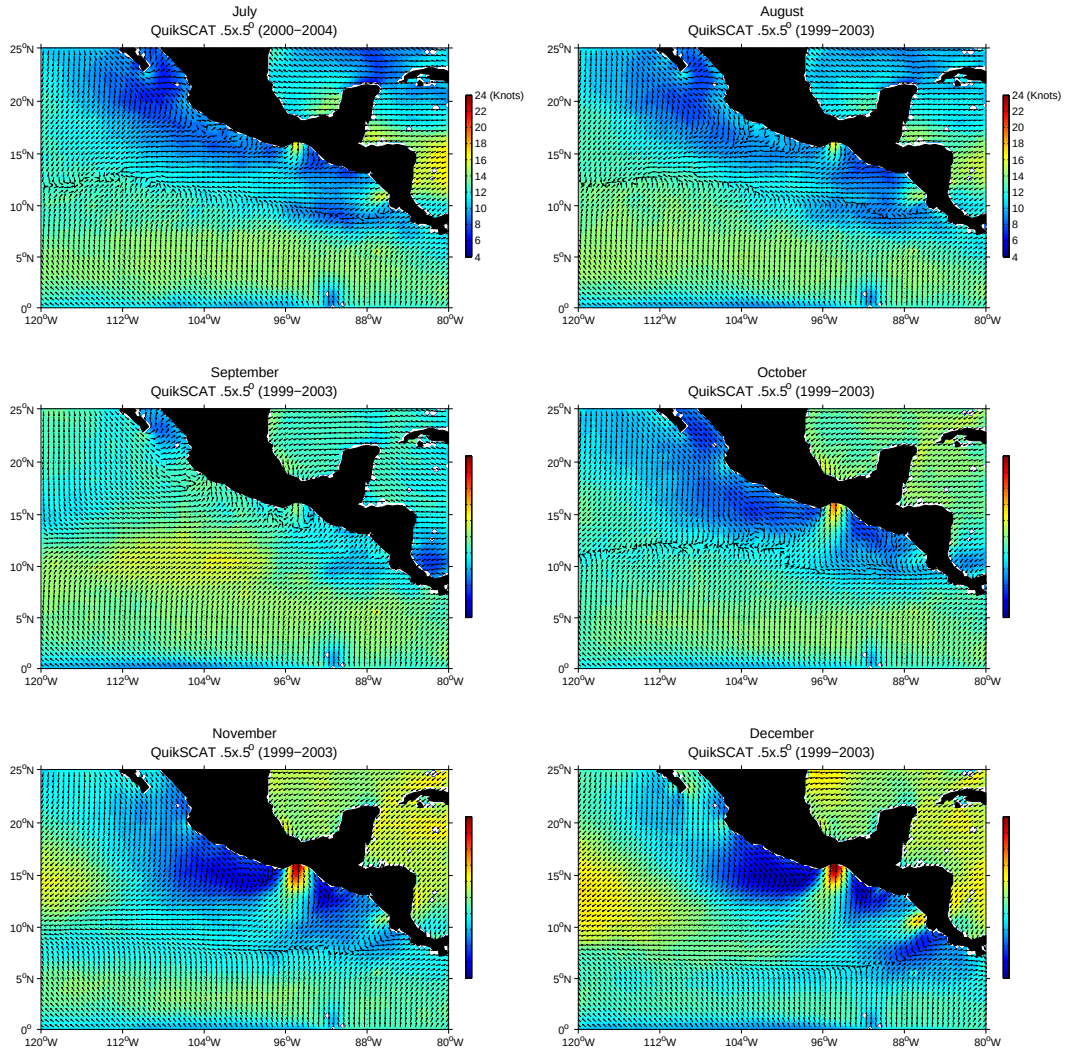

Figure 33. The same as Figure 34 expect for the monthly composite for July (top-left panel) through to December (bottom-right panel).

Figures 32 and 33 show the 5-year monthly composite averages of wind speed and direction off Central America. The Tehuantepec gap winds are clearly visible in these climatological maps. This is especially true for the months of November through January. A secondary maximum of the Tehuantepec winds is evident in the July and August maps. Also visible are the Papagayo gap winds. For the month of December, these climatological Tehuanos and Papagayos show climatological average wind speed maxima of about 13 $m.s^{-1}$ and 8 $m.s^{-1}$ respectively. This average Tehuanos wind speed maximum is comparable with the findings of Xie *et al*. (2005). The wind

speeds during individual events are much stronger than there climatological averages. The February maximum in the Papagayos, described by Chelton *et al*. (2000a), is clearly visible in Figure 32. Both the meridionaly oriented Tehuanos and zonaly oriented Papagayos extend several hundred kilometers offshore before merging with the Pacific northeast trade winds.

Oceanic and Biological Responses

Papagayo gap winds produce two lobes of wind stress curl extending off the coast: an anticyclonic lobe on the poleward side of the wind speed core and a stronger cyclonic lobe on the equatorward side. A similar pattern of wind stress curl is produced by Tehuantepec gap winds. An important difference between these two wind stress curl patterns is that the lobe of cyclonic curl on the equatorward side of the Papagayo gap wind is adjacent to the band of cyclonic curl on the northern side of the ITCZ (Kessler, 2002). Both Xie *et al*. (2005) and Fiedler (2002) show for the months of February through April a shoaling of the thermocline from the Central American coast to about 90°W. This shoaling is associated with the annual cycle of the Costa Rica Dome centered near 9°N, 90°W (Fiedler, 2002) and results from the strong Ekman pumping associated with the cyclonic wind stress curl of the Papagayos gap wind (Xie *et al*., 2005).

The Tehuantepec and Papagayo gap winds have a marked effect on the underlying SST field. During December, SST minima are found to be roughly aligned with the axes of these gap winds (Figure 29). This cooling, which results from increased surface heat flux and vertical mixing (Xie *et al*., 2005), is more apparent within the Gulf of Tehuantepec where wind events are stronger and the minimum SST is about 22°C against a background SST field of up to 30°C (Figure 29).

Vertical mixing and Ekman pumping in the surface ocean below the Tehuantepec and Papagayo gap wind maxima, result in the entrainment of nutrient rich waters from depth (Trasviña *et al*., 1995). This in turn enhances biological productivity as evidenced by the monthly mean fields of SeaWiFS chlorophyll concentration presented in Fiedler (2002). Fiedler (2002) shows a similar enhancement in productivity near the Costa Rica Dome, apparently associated with the shoaling of the thermocline that brings cold, nutrient rich water close to the surface. The shoaling of the thermocline, combined with wind mixing, acts to introduce nutrients into the surface layer. This region of high productivity supports a large zooplankton biomass as well as higher trophic animals such as common dolphins (*Delphinus delphis*) and blue whales (*Balaenoptera musculus*) (Fiedler, 2002).

Gap winds in other regions

Gap winds are observable elsewhere in COGOW. These winds are mostly associated with island chains such the Hawaiian Islands (Figure 34) and the Canary Islands (Figure 35) off northwest Africa. In a similar way to the Central American winds described above, these gap winds contain clear annual cycles with both regions exhibiting a boreal summertime maximum.

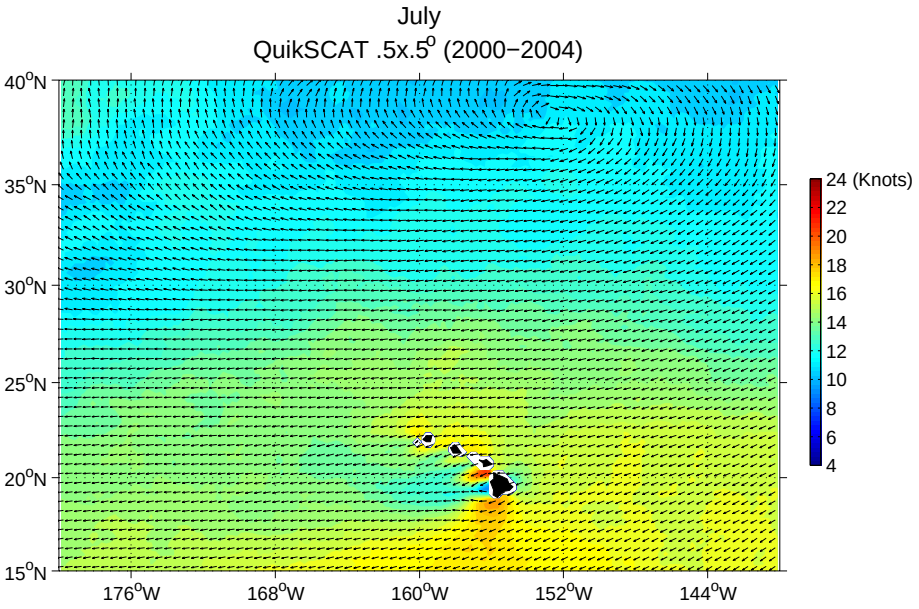

Figure 34. 5-year (2000-2004) monthly composite average of the wind field at 10 m derived from the QuikSCAT scatterometer for July. Scalar averaged wind speed is shown in color on a 0.25° x 0.25° grid. Vector averaged climatological wind directions are plotted as unit vectors on a 0.5° x 0.5° grid.

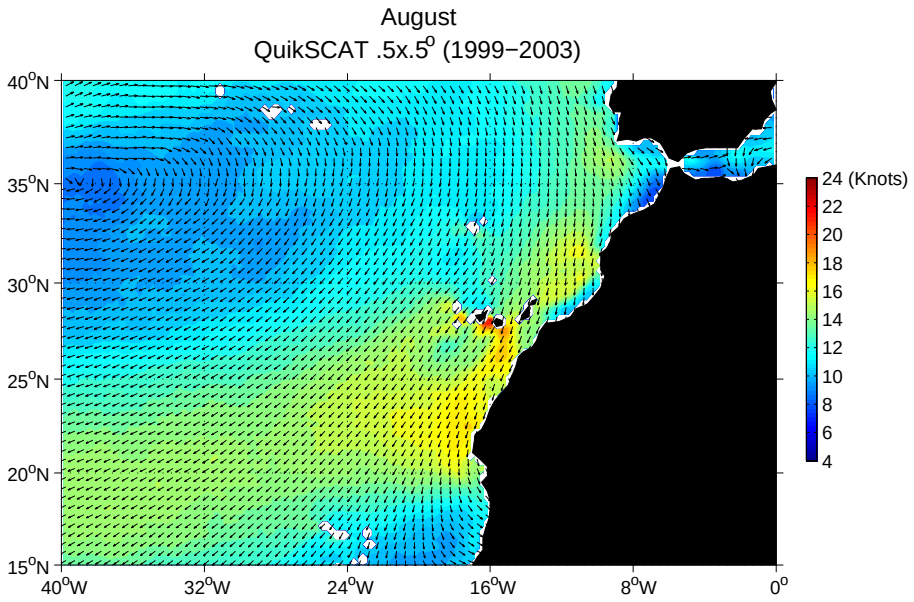

Figure 35. The same as Figure 34 expect for the monthly composite for August (1999-2003) off the west coast of North Africa.

Corner Accelerations

Greenland

The world's largest island, Greenland is about three times the size of Texas. Its topography is characterized by an icecap that rises dramatically from sea-level to exceed 3,000 m in the east-central interior (Figure 36). This complex and steep topography has a significant impact on both the regional surface wind field (Doyle and Shapiro, 1999; Moore and Renfrew, 2005) and the general circulation of the Northern Hemisphere at lower and mid-tropospheric levels (Petersen *et al*., 2004). Arguably, one of the most dramatic modifications of the surface wind field by Greenland's large-scale topography are the episodic corner accelerations or "tip jets" and "reverse tip jets" that form off Cape Farewell, located at the southern tip of Greenland (Moore, 2003). These low-level jets, which can reach speeds greater than 30 $m.s^{-1}$ (Figure 36), and the associated wave fields, pose a considerable hazard to, amongst other things, commercial ship traffic (Khandekar and Swail, 1995).

Westerly corner accelerations are triggered by the passage of synoptic-scale extra-tropical cyclones to the northeast of Cape Farewell (Moore, 2003). These accelerations result from the combined effect of the conservation of the Bernoulli function during orographic descent and acceleration due to flow splitting as stable air rounds Cape Farewell (Doyle and Shapiro, 1999). Pickart *et al*. (2003) have recently identified these westerly corner accelerations as being an important forcing for localized deep ocean convection in the southern Irminger Sea through elevated heat flux. This region is considered to provide an additional source of the so-called "Labrador Sea Water" (Pickart *et al*., 2003).

Using 10 m NCEP reanalysis wind fields to develop a climatology of high wind speed events near Cape Farewell, Moore (2003) presents the so-called "reverse tip jet" phenomenon. These easterly corner accelerations are associated with the interaction between the high topography of southern Greenland and synoptic-scale extra-tropical cyclones situated to the south of Cape Farewell (Moore, 2003).

An example of each class of corner acceleration events is presented in Figure 36. The top panel of Figure 36, 5 November 2004, shows a reverse corner acceleration. The botttom panel, 29 November 2004, shows a corner acceleration resulting from westerly flow. Time series of zonal wind velocities for five consecutive Novembers (2000-2004) measured four times daily at the Prins Christian Sund weather station (60.03°N 43.12°W) are shown in Figure 37. The temporal characteristics of the events shown in Figure 36 are evident in the bottom panel of Figure 37.

The bottom panel of Figure 36 shows a westerly corner acceleration event that has zonal and meridional extents of about 1000 km and 250 km respectively. This fan-shaped region of high wind speeds is asymmetrical in that the horizontal shear along its southern border is significantly weaker than along its northern border. The wind speed maximum (> 30 $m.s^{-1}$) for this event is located south of Cape Farewell.

The top panel of Figure 36 shows an easterly corner acceleration event. This event has a markedly different structure to that of the westerly acceleration. Along the southeast coast of Greenland, there appears to be topographically induced barrier flow, similar to the one described in Moore and Renfrew (2005), as the cyclonic circulation interacts with the Greenland coastline. Similar barrier flows are observed elsewhere when cyclones interact with topographic barriers (O'Connor *et al*., 1994). The region of strongest winds is confined to within 400 km of the east coast before wrapping around Cape Farewell into the Labrador Sea to the west. The wind speed

maximum (> 30 $m.s^{-1}$) is located to the southeast of Cape Farewell. Moore and Renfrew (2005) propose that such easterly corner accelerations occur when barrier winds reach the barrier end and move from a geostrophic to a gradient wind balance, becoming supergeostrophic as a result of their anticyclonic curvature.

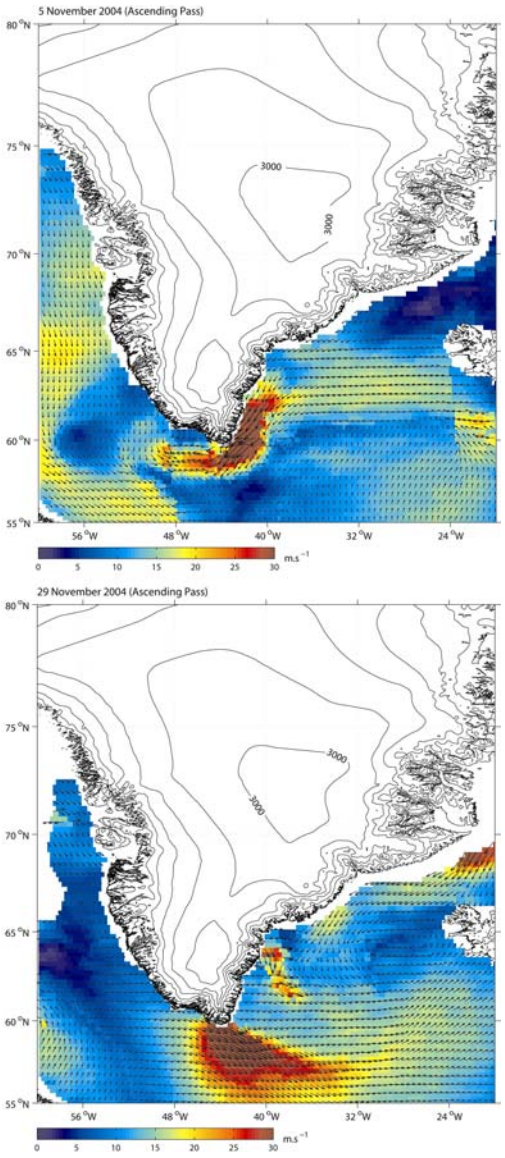

Figure 36. Daily (5 and 29 November 2004) composites of the wind field at 10 m derived from the QuikSCAT scatterometer. Scalar averaged wind speed is shown in color on a 0.25° x 0.25° grid. For presentation purposes every second vector is plotted, i.e. the vectors are plotted on a 0.5° x 0.5° grid. The top panel shows a reverse corner acceleration event. The bottom panel shows a corner acceleration event. The topography of Greenland is plotted with a contour interval of 500 m in both panels.

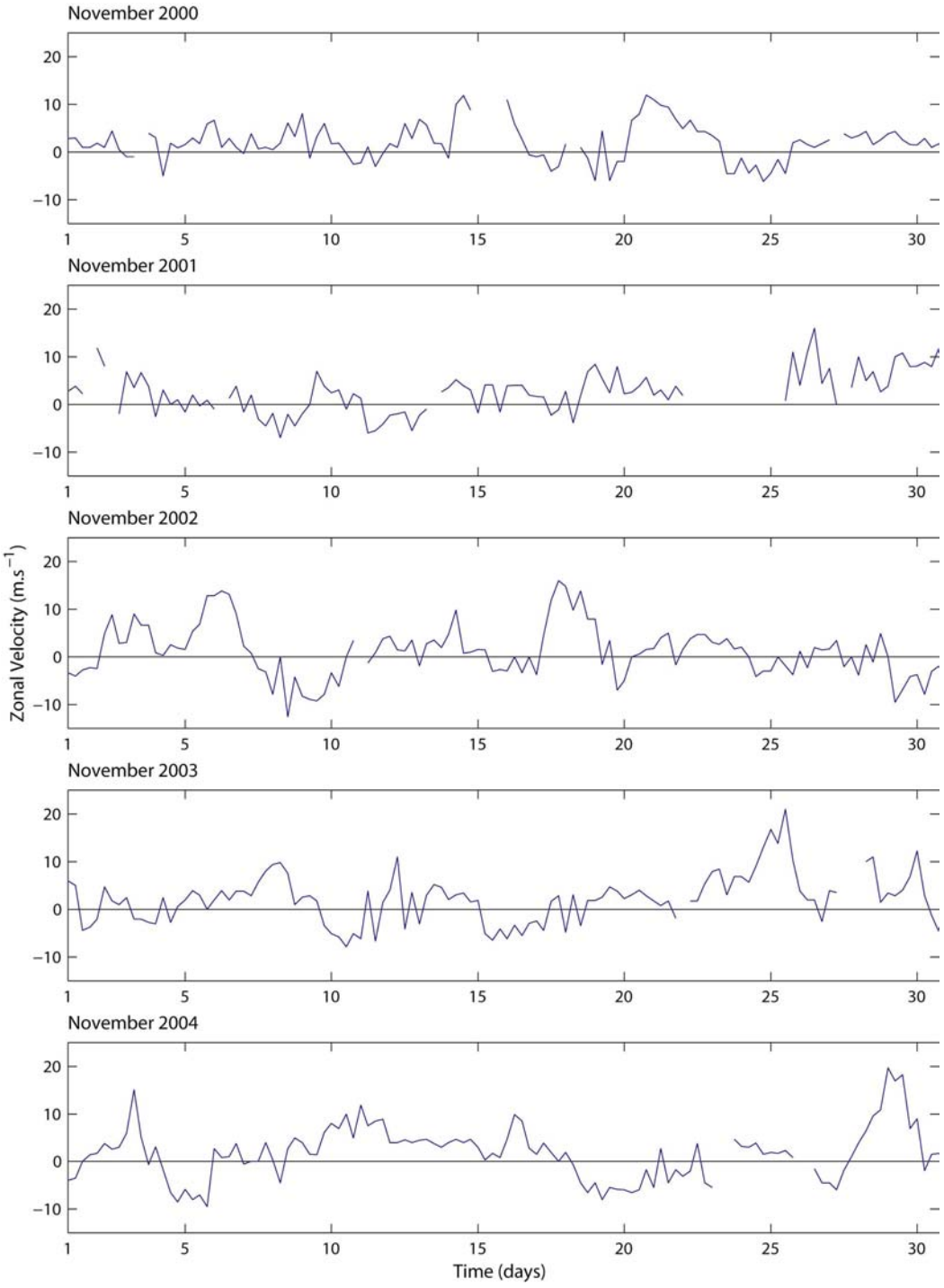

Figure 37. Zonal wind velocity (m.s^{-1}) for the month of November 2000-2004. These data are derived from the Prins Christian Sund weather station (60.03°N 43.12°W). This weather station is located 74 m above sea-level. Data are recorded every six hours (gaps indicate missing data).

Pickart *et al*. (2003) provide evidence that the occurrence of such corner and reverse corner accelerations is tied to the North Atlantic Oscillation (NAO) Index. Using a 35-year time series, derived from the Prins Christian Sund weather station, these authors find a statistically significant relationship whereby a positive NAO Index implies more frequent acceleration events. Moore (2003) supports these findings. He finds that the probability of observing an acceleration event during a winter month in which the NAO Index is positive is about 14 %. In contrast, the probability during a winter month in which the NAO Index is negative is only 5 %.

While these corner acceleration events occur at synoptic timescales of two to five days (Figure 37), they are of sufficient magnitude for them to be clearly visible in the 5-year QuikSCAT climatology presented in Moore and Renfrew (2005).

Figure 38 depicts the COGOW 5-year monthly composite average of wind speed and direction for November. The Greenland corner acceleration is visible in this climatological map as a wind speed maximum in excess of 24 knots (~ 12 $m.s^{-1}$) located south-southeast of Cape Farewell. Since reverse corner accelerations are less frequent, the climatological mean wind field is dominated by the flow characteristics of northwesterly corner accelerations. Both classes of corner accelerations are, however, captured in the wind rose plots, an example of which is given in Figure 39. This November (1999-2003) wind rose centered at 58.75°N 44.25°W (highlighted by center of the white circle south of Greenland in Figure 38) shows a bimodal distribution with winds coming most frequently from either the west-northwest and northwest (~ 37 %) or the north-northeast and northeast (~ 17.5 %) at speeds greater than 15 knots. These data are in reasonable agreement with the wind rose plots presented in Moore and Renfrew (2005). Using QuikSCAT winter (DJF 1999-2004) observations at Cape Farewell (59.375°N, 42.875°W), Moore and Renfrew (2005) show a bimodal wind regime with winds coming most frequently from the either the west and west-northwest or the north-northeast and northeast.

Based on the 35-year time series mentioned above, Pickart *et al*. (2003) found these events to be strongly seasonal, occurring from late autumn through early spring. However, the COGOW climatology reveals that a local wind speed maximum exists south of Cape Farewell for every month other than July and August (not shown). Although this maximum is present during the winter months, it is not visually clear in COGOW due to the fact that the dynamic range of the colorbar saturates at 24 knots.

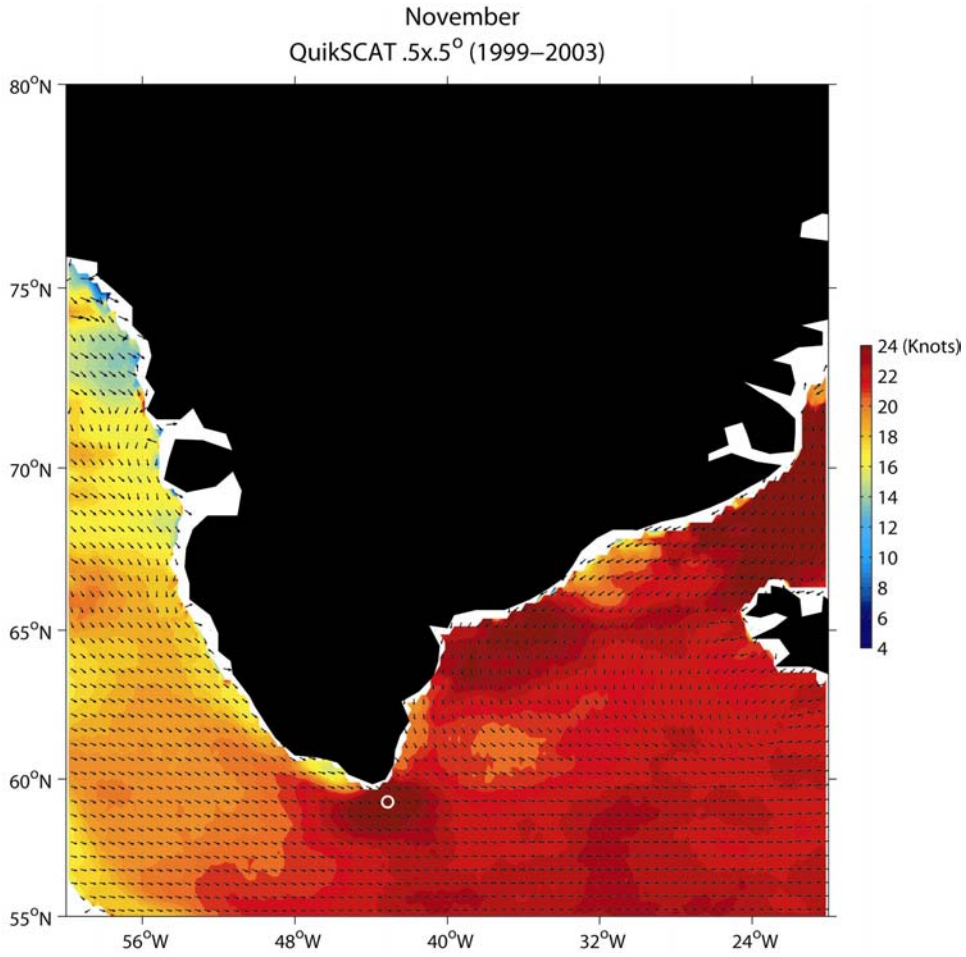

Figure 38. 5-year (1999-2003) monthly composite average of the wind field at 10 m derived from the QuikSCAT scatterometer for November. Scalar averaged wind speed is shown in color on a 0.25° x 0.25° grid. Vector averaged climatological wind directions are plotted as unit vectors on a 0.5° x 0.5° grid. The center of the white circle, south of Cape Farewell, highlights the location of the wind rose plot shown in Figure 39.

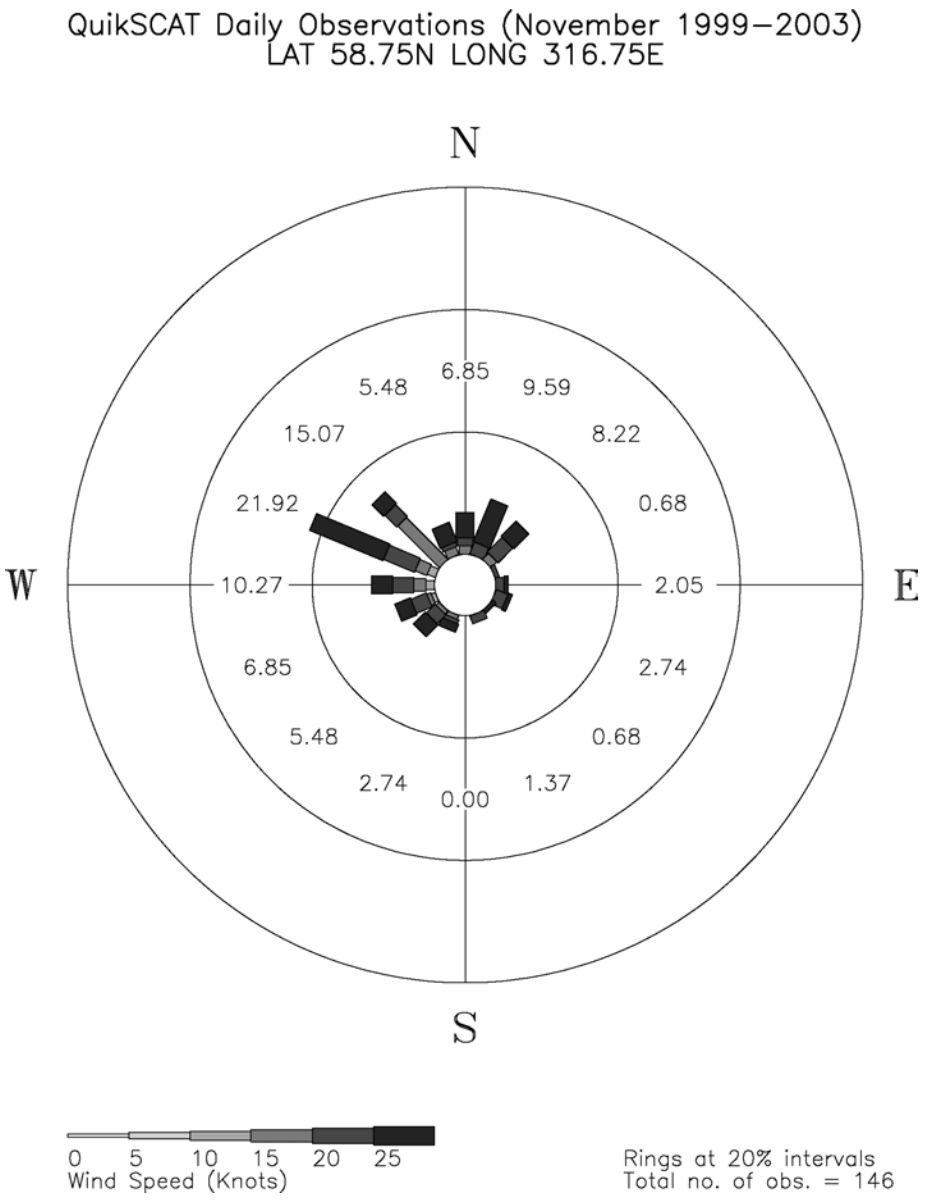

Figure 39. Wind rose plot for the month of November (1999-2003) for a 0.5° x 0.5° area centered at 58.75°N 44.25°W. The center of the white circle, south of Cape Farewell in Figure 38 highlights this position.

Madagascar

Similar examples of corner accelerations can be found elsewhere within COGOW. One such example occurs off the coast of Madagascar (Figure 40), which is a particularly interesting example because accelerations occur off both the northern and southern tip of the island. For the month of October, the northern maximum is marginally stronger and less variable than its southern counterpart with a 5-year mean wind speed of about 20 knots.

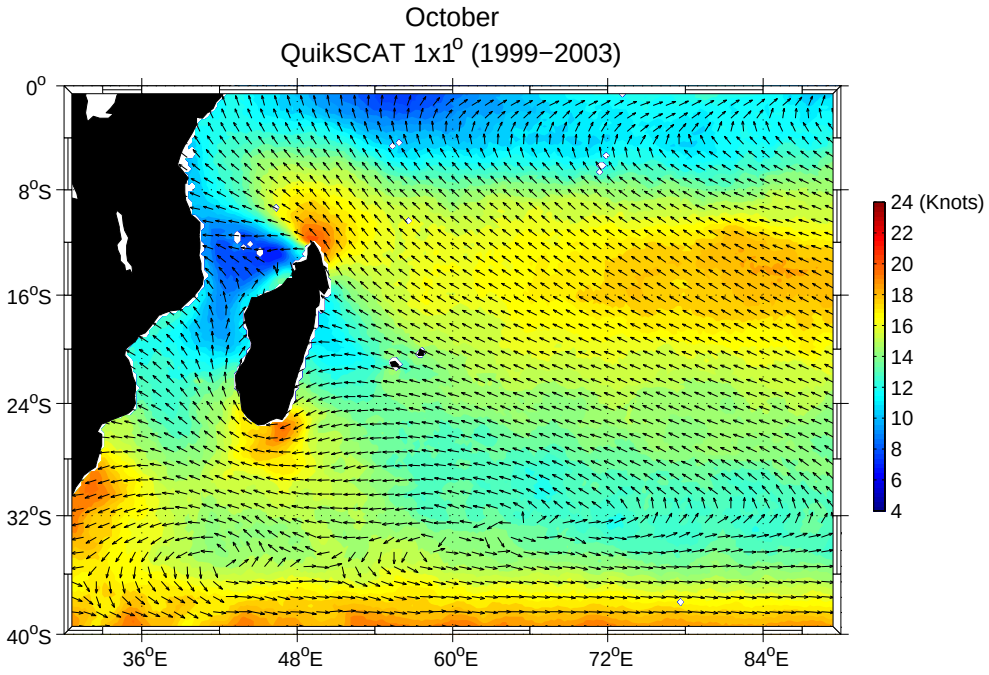

Figure 40. 5-year (1999-2003) monthly composite average of the wind field at 10 m derived from the QuikSCAT scatterometer for October. Scalar averaged wind speed is shown in color on a 0.25° x 0.25° grid. Vector averaged climatological wind directions are plotted as unit vectors on a 1° x 1° grid.

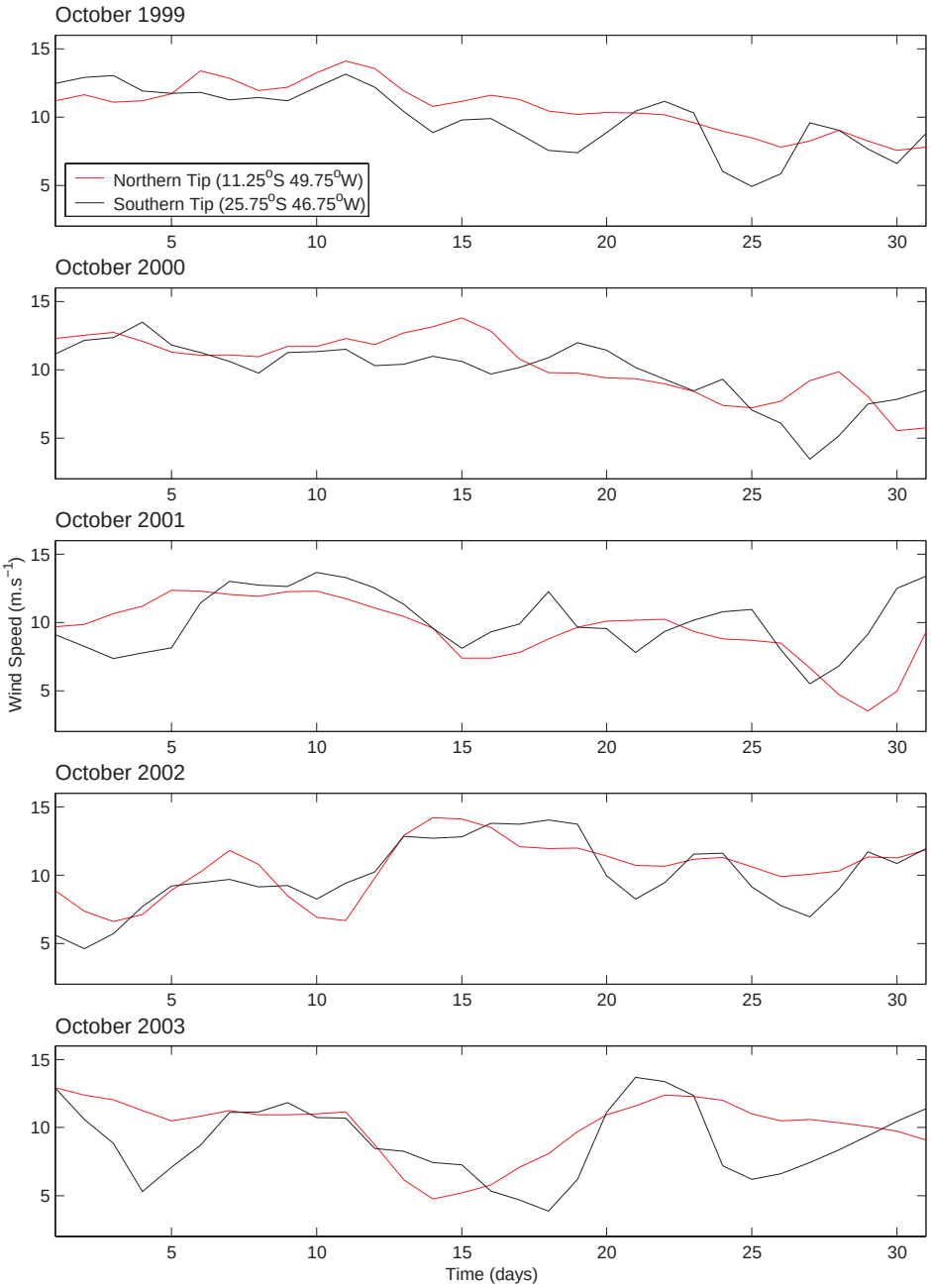

Figure 41. 5-year October (1999-2003) climatology of 10 m wind speeds ($m.s^{-1}$) derived from the QuikSCAT scatterometer for two 0.5° x 0.5° areas centered at 11.25°S 49.75°W and 25.75°S 46.75°W. These data are derived from 3-day composite QuikSCAT wind fields.

Figure 41 shows wind speed data for five successive Octobers (1999-2003), derived from the 3-day composite QuikSCAT wind fields for locations centered within each of the corner accelerations. A strong tendency for synchronous occurrence of these two corner accelerations is evident from this figure. An example of this synchroneity is also shown in Figure 42 from the 3-day composite QuikSCAT wind field for 14-16 October 2002. This event is clearly captured in the two 5-year time series presented in the October 2002 panel in Figure 41. Figure 42 shows wind speed maxima off the northern (11.25°S 49.75°W) and southern (25.75°S 46.75°W) tips of Madagascar. Along the south coast, the east-southeasterly to easterly winds are strongly upwelling favorable in that they would induce an Ekman drift to the south. Figure 43 shows a 7-day composite (centered on 16 October 2002) of interpolated AVHRR SST anomalies derived from the NOAA-16 satellite. In it there is evidence of localized upwelling along Madagascar's southeast coastline. The 7-day composites of SST anomalies preceding and following this event (not shown) reveal little or no localized upwelling.

Using SeaWiFS ocean color data, AVHRR SST data and wind fields derived from the ERS-2 satellite, Lutjeharms and Machu (2000) document an upwelling event, similar to the one depicted in Figures 42 and 43, which occurred on 12 October 1997. Even though the winds for the preceding seven days were upwelling favorable, these authors conclude that this upwelling cell was probably not wind-driven. In fact, after investigating all SeaWiFS level-2 images for 1998, Lutjeharms and Machu (2000) found no pattern between ERS-2 derived winds and localized upwelling events off the southeast coast of Madagascar. These authors therefore conclude that upwelling in this region is the result of topographical forcing (Lutjeharms *et al*., 1989) by the western boundary East Madagascar Current (DiMarco *et al*., 2002).

The conclusions of Lutjeharms and Machu (2000) differ from those of DiMarco *et al*. (2000), who investigate wind-stress and AVHRR SST over the continental slope and shelf of southern Madagascar for February and March 2000. DiMarco *et al*. (2000)

show localized upwelling off southern Madagascar that occurs concurrently with high, upwelling favorable, pseudo wind-stress. Unlike Lutjeharms and Machu (2000), DiMarco *et al*. (2000) hypothesize that this upwelling is forced through a combination of anomalously strong, upwelling-favorable wind-stress and topographical forcing. The climatology presented here shows support for the hypothesis of DiMarco *et al*. (2000). COGOW shows that for October (1999-2003) the winds off southern Madagascar (26.25°S 46.75°E) are mostly upwelling favorable, i.e. they blow from the east, east-northeast or northeast about 60 % of the time.

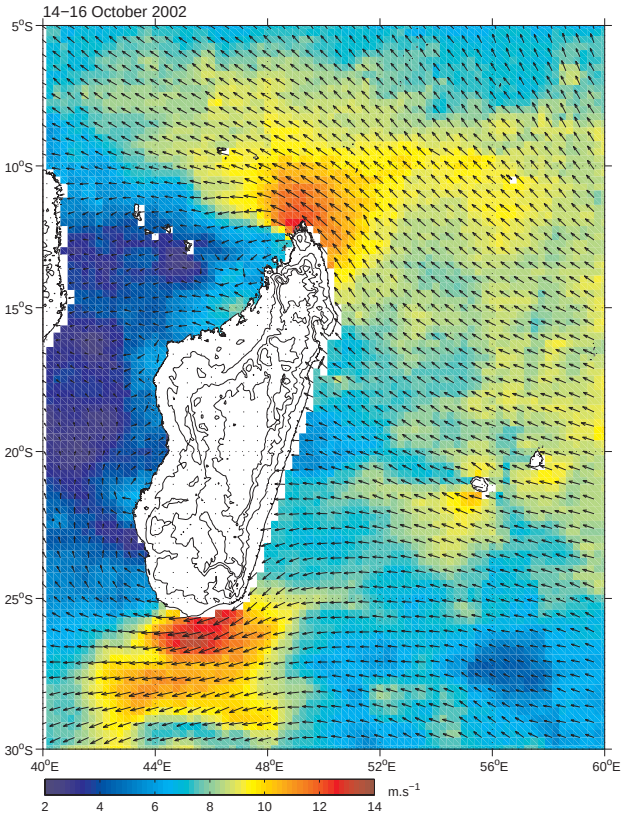

Figure 42. 3-day composite average of the wind field at 10 m derived from the QuikSCAT scatterometer for 14-16 October 2002. Scalar averaged wind speed is shown in color on a 0.25° x 0.25° grid. For presentation purposes, vector averaged wind directions are plotted on a 0.5° x 0.5° grid. The topography of Madagascar is plotted with a contour interval of 400 m.

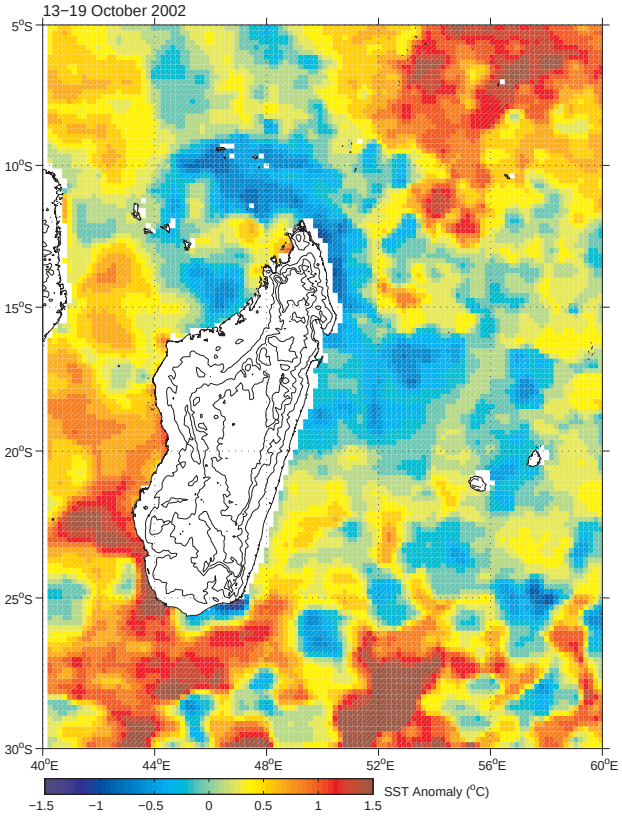

Figure 43. Interpolated AVHRR multichannel SST composite anomalies for 13-19 October 2002. These data are plotted on a 18 km square grid. The topography of Madagascar is plotted with a contour interval of 400 m.

Chapter 5: Potential User Groups

Knowledge of offshore wind climatologies is of critical importance to the marine operational and research communities alike. Several examples of potential user groups are discussed below. This list is not intended to be comprehensive.

The Climatology of Global Ocean Winds will be of use to oil spill responders both nationally here in the U.S., as evidenced by OR&R's involvement in the recovery of *Ehime Maru*, and internationally in isolated and remote regions such as the Galapagos Islands (Sanderson *et al*., 2001). In addition, COGOW could be used for oil spill contingency planning purposes. For example, the Australian National Marine Oil Spill Contingency Plan (NMOSCP) states that knowledge of, 'wind speed and direction at spill locations is vital to the effectiveness of the spill simulation model' (NMOSCP, 2005: 96). Another example of the need for high quality wind speed and direction data is given by the International Petroleum Industry Environmental Conservation Association (IPIECA), a voluntary non-profit organization whose membership includes both petroleum companies and associations at regional, national and international levels. The IPIECA (2000) suggests, in their Guide to Contingency Planning for Oil Spills on Water, that an oil spill contingency plan should be comprised of, amongst other things, a data directory. In their opinion, such a directory ought to contain relevant coastal charts that include, along with current and tidal data, prevailing wind data. COGOW fulfills such a need.

COGOW is also of potential use to the private sector and resource managers planning development of offshore wind power technologies. Musial and Butterfield (2004) estimate the wind energy potential to be in excess of 3 giga-watts (GW)[7] in the region

[7] The total U.S. electrical generation capacity for all fossil, nuclear and renewable generation is 914 GW (http://www.eere.energy.gov/windandhydro/windpoweringamerica/pdfs/workshops/2005_summit/musial.pdf)

between 20 and 50 nautical miles (about 35-90 km) offshore of California and the Pacific Northwest, a region that is resolved in the QuikSCAT dataset presented here.

Roper (2004) identifies the key parameters in predicting the trajectory of a Search and Rescue (SAR) object as being mean surface wind and current velocities and their variability, the above- and below-water profile of the drifting object, and the last known position of the object. For most SAR operations such data should be available within 4 hours of the incident (Roper, 2004). The spatial resolution required depends upon the nature of the SAR object. For example, survival craft require lower resolution data than persons floating in the water. Presently however, the Canadian Meteorological Center is only able to supply the Canadian Coast Guard with model wind fields on a 2° latitude by 2° longitude grid south of 60°N and on a 2° latitude by 4° longitude grid over the Arctic (Roper, 2004). While COGOW at present only provides climatological wind data, which are not suitable for real-time SAR operations, it is able to provide these data at a considerably higher spatial resolution (0.5° latitude by 0.5° longitude grid) than that of the Canadian Meteorological Center. COGOW could therefore be of use to SAR teams such as the U.S. and Canadian Coast Guards in terms of assisting them with SAR training exercises and contingency planning. It is hoped that a future version of COGOW will include the option to overlay a near real-time (NRT) vector, derived from QuikSCAT wind observations, on top of each of the QuikSCAT climatological wind rose plots. In addition, such a feature could be of significant value to commercial maritime industries. For example, with NRT capabilities COGOW could be incorporated into, for example, NOAA's Physical Oceanographic Real Time System (PORTS), which is a decision support tool that is designed to improve navigation safety and efficiency http://140.90.121.76/d_ports.html). PORTS is just one of the marine navigation services offered by NOAA’s National Ocean Service.

Chapter 6: Summary

While it is clear that knowledge and understanding of global ocean winds is important at many levels within our society, this comprehension has historically been hindered by poor *in situ* coverage by buoys and ships alike. The result was that vast portions of the global ocean have been severely under sampled, both temporally and spatially. Since July 1999 this situation has changed significantly. Through high-resolution spatial sampling and frequent temporal sampling by NASA's QuikSCAT satellite, launched in June 1999, approximately 90 % of global ocean vector winds are now sampled daily at a 25 km resolution.

The Climatology of Global Ocean Winds (COGOW) is a 5-year (August 1999 - July 2004) climatology of the QuikSCAT dataset. While other published climatologies of global ocean winds exist (e.g., the Marine Climatic Atlas of the World), COGOW provides, within the limitations of the 5-year duration of this dataset, the first high spatial resolution, observationally based, online atlas of global ocean winds.

The utility of COGOW is introduced by way of a case study of NOAA OR&R's involvement in recovery efforts of *Ehime Maru*, a Japanese training and fishing vessel that sank south of the island of Oahu on 9 February 2001 after it collided with the USS *Greeneville*. This case study shows that the 10 knot constant wind speed used by OR&R in their oil spill trajectory analyses, when compared with COGOW, significantly underestimated the average wind speeds south of Oahu. COGOW shows these winds to contain low directional variability, blowing predominantly from the east or east-northeast at speeds of between 15 and 20 knots. Such information could have proven vital, with regards to oil spill mitigation, had the fuel tanks of Ehime Maru ruptured during this recovery operation.

Chapter 4 introduced examples of phenomena that are visible within COGOW. Discussions of the south Asian monsoon, SST and wind field coupling, gap winds and corner accelerations, were included to provide users with various starting points from which to explore the COGOW atlas of ocean winds. While these discussions focus on the climatological wind fields contained within COGOW, they also contain various historical asides as well as discussions of associated phenomena such as oceanic and biological response to wind forcing. These tangential discussions were included to place these phenomena in greater physical and cultural contexts, as well as in an attempt to pique reader interest in a particular phenomenon, or an aspect of that phenomenon, thereby potentially enticing the reader to possibly conduct more in-depth personal research. Chapter 5 provides a non-comprehensive list and discussion of potential user groups.

Acknowledgements

The QuikSCAT data presented here are produced by Remote Sensing Systems and sponsored by the NASA Ocean Vector Winds Science Team (http://www.remss.com).

The Gridded 18km MCSST Level 3 (NAVOCEANO) and 4km MODIS datasets were obtained from the Physical Oceanography Distributed Active Archive Center (PO.DAAC) (http://podaac.jpl.nasa.gov).

NCEP Reanalysis sea-level pressure and surface precipitation rate fields were obtained from the NOAA-CIRES Climate Diagnostics Center (http://www.cdc.noaa.gov).

The All-India monsoon rainfall index data and Prins Christian Sund wind data w provided by Dr. B. Parthasarathy of the Indian Institute of Tropical Meteorology (http://grads.iges.org/india/allindia.html) and the Russian Weather Server (http://meteo.infospace.ru/wcarch/html/e_day_stn.sht?stn=297) respectively.

This work was prepared with partial support from award NA03NES4400001 to Oregon State University's Cooperative Institute for Oceanographic Satellite Studies from the National Oceanic and Atmospheric Administration, U.S. Department of Commerce. NASA grant NAS5-32965 for funding of Ocean Vector Winds Science Team activities provided additional support for this research. The statements, findings, conclusions, and recommendations expressed in this manual are those of the author, Craig M. Risien, and do not necessarily reflect the views of the National Oceanic and Atmospheric Administration, the U.S. Department of Commerce or the National Aeronautics and Space Administration.

Bibliography

Annamalai, H., and J. M. Slingo, 2001. Active/break cycles: diagnosis of the intraseasonal variability of the Asian Summer Monsoon. *Climate Dynamics*, 18(1-2), 85-102

Bang, N. D., 1970. Dynamic interpretations of a detailed surface temperature chart of the Agulhas Current retroflexion (sic) and fragmentation area. *S. Afr. Geograph. J.*, 52, 67-76

Baars, M. A., P. H. Schalk, and M. J. W. Veldhuis, 1998. Seasonal fluctuations in plankton biomass and productivity in the ecosystems of the Somali Current, Gulf of Aden, and southern Red Sea. In: Sherman, K., E. N. Okemwa and M. J. Ntiba (*eds*.), Large Marine Ecosystems of the Indian Ocean: Assessment, Sustainability, and Management. Blackwell Scientific, Malden, MA, pp. 143-174

Belkin, I. M., and A. L. Gordon, 1996. Southern Ocean fronts from the Greenwich meridian to Tasmania. *J. Geophys. Res.*, 101, 3675-3696

Boebel, O., C. Duncombe Rae, S. Garzoli, J. Lutjeharms, P. Richardson, T. Rossby, C. Schmid, and W. Zenk, 1998. Float experiment studies interocean exchanges at the tip of Africa. *EOS*, 79(1), 6-8

——, H. T Rossby, J. R. E. Lutjeharms, W. Zenk, and C. Barron, 2003. Path and variability of the Agulhas Return Current. *Deep-Sea Res.*, 50(1), 35-56

Bourassa, M. A., L. Zamudio, and J. J. O'Brien, 1999. Non-inertial flow in NSCAT observations of Tehuantepec winds. *J. Geophys. Res.*, 104, 11,311-11,320

Bryden, H. L., L. M. Beal, and L. M. Duncan, 2005. Structure and Transport of the Agulhas Current and Its Temporal Variability, *J. Oceanog.*, 61(3), 479-492

Chapel, L. T., 1927. Winds and storms on the Isthmus of Panama. *Mon. Wea. Rev.*, 55, 519-530

Chelton, D. B., S. K. Esbensen, M. G. Schlax, N. Thum, M. H. Freilich, F. J. Wentz, C. L. Gentemann, M. J. McPhaden, and P. S. Schopf, 2001. Observations of coupling between surface wind stress and sea surface temperature in the eastern Tropical Pacific. *J. Climate*, 14, 1479-1498

——, and M. H. Freilich, 2005. Scatterometer-based assessment of 10-m wind analyses from the operational ECMWF and NCEP numerical weather prediction models. *Mon. Wea. Rev.*, 133, 409-429

——, ——, and S. K. Esbensen, 2000a. Satellite observations of the wind jets off the Pacific coast of Central America, Part I: Case studies and statistical characteristics. *Mon*. *Wea*. *Rev*., 128, 1993-2018

——, —— and, ——, 2000b. Satellite observations of the wind jets off the Pacific coast of Central America, Part II: Regional relationships and dynamical considerations. *Mon*. *Wea*. *Rev*., 128, 2019-2043

——, ——, J. M. Sienkiewicz, and J. M. Von Ahn, 2006. On the use of QuikSCAT scatterometer measurements of surface winds for marine weather prediction. *Mon*. *Wea*. *Rev*., Submitted

——, M. G. Schlax, M. H. Freilich, and R. F. Milliff, 2004. Satellite measurements reveal persistent small-scale features in ocean winds. *Science*, 303, 978-983

Department of the Navy, 2001. *Ehime Maru* Environmental Assessment: Finding of no Significant Impact (http://www.smdcen.us/pubdocs/)

DiMarco, S. F., P. Chapman, and W. D. Nowlin Jr., 2000. Satellite observations of upwelling on the continental shelf south of Madagascar. *Geophys*. *Res*. *Lett*., 27, 3965-3968.

——, ——, ——, P. Hacker, K. Donohue, M. Luther, G. C. Johnson, and J. Toole, 2002. Volume transport and property distributions of the Mozambique Channel. *Deep-Sea Res*., 49,1481-1511

Doyle, J. D., and M. A. Shapiro, 1999. Flow response to large-scale topography: The Greenland tip jet. *Tellus*, 51A, 728-748

Fiedler, P. C., 2002. The annual cycle and biological effects of the Costa Rica Dome. *Deep-Sea Res*., 49A, 321-338

Findlater, J., 1969. A major low-level current near the Indian Ocean during the northern summer. *Quart*. *J*. *Roy*. *Meteor*. *Soc*. *London*, 95, 362-380

——, 1971. Mean monthly airflow at low levels over the western Indian Ocean. *Geophys*. *Memoirs*, 115, 1-53

Freilich, M. H., 1997. Validation of vector magnitude datasets: Effects of random component errors. *J*. *Atmos*. *Oceanic*. *Technol*., 14, 695-703
——, and R. S. Dunbar, 1999. The accuracy of the NSCAT-1 vector winds: Comparisons with National Data Buoy Center buoys. *J*. *Geophys*. *Res*., 104, 11,231-11,246

——, D. G. Long, and M. W. Spencer, 1994. SeaWinds: A scanning scatterometer for ADEOS II - Science overview. *Proc. Int. Geoscience and Remote Sensing Symp*., Pasadena, CA, IEEE, 960-963

Gadgil, S., 1996. Climate Change and Agriculture-An Indian perspective, in Climate Variability and Agriculture, Y. P. Abrol, S. Gadgil, and G. B. Pant (*eds*.), Narosa, New Delhi, India, pp. 1-18

——, 2003. The Indian monsoon and its variability. *Annu*. *Rev*. *Earth Planet*. *Sci*., 31, 429-467

——, and P. V. Joseph, 2003. On breaks of the Indian monsoon. *Proc*. *Indian Acad*. *Sci*. *(Earth Planet*. *Sci.)*, 112(4), 529-558

Halley, E., 1686. An historical account of the trade winds and monsoons observable in the seas between and near the tropics with an attempt to assign a physical cause of the said winds. *Philos*. *Trans*. *Roy*. *Soc*. *London*,16, 153-168

Hurd, W. E., 1929. Northers of the Gulf of Tehuantepec. *Mon*. *Wea*. *Rev*., 57, 192-194

International Petroleum Industry Environmental Conservation Association, 2000. A Guide to Contingency Planning for Oil Spills on Water. http://www.ipieca.org/downloads/oil_spill/oilspill_reports/English/Vol2_ContPlanning_1050.71KB.pdf

Joseph, P. V., and S. Sijikumar, 2004 Intraseasonal variability of the low-level jet stream of the Asian summer monsoon. *J*. *Climate*, 17, 1449-1458

Jury M. R., and N. Walker, 1988. Marine boundary layer modification across the edge of the Agulhas Current. *J*. *Geophys*. *Res*., 93, 647-654

Kanamitsu, M., 1989. Description of the NMC global data assimilation and forecast system. *Wea*. *Forecasting*, 4, 335-243

Kalnay, E., and Coauthors, 1996. The NCEP/NCAR 40-year reanalysis project, *Bull*. *Am*. *Meteorol*. *Soc*., 77, 437-471

Kessler, W. S., 2002. Mean three-dimensional circulation in the northeast tropical Pacific. *J*. *Phys*. *Oceanogr*., 32, 2457-2471

Khandekar, M. L., and V. R. Swail, 1995. Storm waves in Canadian waters – A major marine hazard. *Atmos*.*–Ocean,* 33, 329-357

Lindzen, R. S., and S. Nigam, 1987. On the role of sea surface temperature gradients in forcing low-level winds and convergence in the Tropics. *J. Atmos. Sci.*, 44, 2418-2436

Lutjeharms, J. R. E., and I. J. Ansorge, 2001. The Agulhas Return Current. *J. Mar. Syst.,* 30, 115-138

——, M. L. Gründlingh, and R. A. Carter, 1989. Topographically induced upwelling in the Natal Bight. *S. Afri. J. Sci.*, 85, 310-316

——, and E. Machu, 2000. An upwelling cell inshore of the East Madagascar Current. *Deep-Sea Res.*, 47(12), 2405-2411

——, and R. C. van Ballegooyen, 1988. The retroflection of the Agulhas Current. *J. Phys. Oceanogr.*, 18, 1570-1583

——, and H. R. Valentine, 1984. Southern Ocean thermal fronts south of Africa. *Deep-Sea Res.*, 31, 1461-1475

Machu, E., and V. Garçon, 2001. Phytoplankton seasonal distribution from SeaWiFS data in the Agulhas Current system. *J. Mar. Res.*, 59, 795-812

Milliff, R. F., J. Morzel, D. B. Chelton, and M. H. Freilich, 2004. Wind stress curl and wind stress divergence biases from rain effects on QSCAT surface wind retrievals. *J. Atmos. Ocean. Technol.*, 21(8), 1216-1231

Moore, G. W. K., 2003. Gale force winds over the Irminger Sea to the east of Cape Farewell, Greenland. *Geophys. Res. Lett.*, 30**,** 1894, doi:10.1029/2003GL018012

——, and I. A. Renfrew, 2005. Tip jets and barrier winds: A QuikSCAT climatology of high wind speed events around Greenland. *J. Climate*, 18, 3713-3725

Musial, W. and S. Butterfield, 2004. Future for Offshore Wind Energy in the United States: Preprint; NREL Report No. CP-500-36313. National Renewable Energy Laboratory, Golden, Colorado. http://www.nrel.gov/docs/fy04osti/36313.pdf

National Climate Data Center, 2001. Data on historical wind speeds at Honolulu International Airport. Asheville, North Carolina

National Marine Oil Spill Contingency Plan: Australia's "National Plan to Combat Pollution of the Sea by Oil and Other Noxious and Hazardous Substances", 2005. http://www.amsa.gov.au/Marine_Environment_Protection/National_plan/Contingency_Plans_and_Management/Oil_Spill_Contingency_Plan.asp

Nonaka, M., and S.-P. Xie, 2003. Covariations of sea surface temperature and wind over the Kuroshio and its extension: Evidence for ocean-to-atmosphere feedback. *J. Climate*, 16, 1404-1413

O'Connor, W. P., D. H. Bromwich, and J. F. Carrasco, 1994. Cyclonically forced barrier winds along the Transantarctic Mountains near Ross Island. *Mon. Wea. Rev.*, 122, 137-150

O'Neill, L. W., D. B. Chelton, and S. K. Esbensen, 2003. Observations of SST-induced perturbations of the wind stress field over the Southern Ocean on seasonal time scales. *J. Climate*, 16**,** 2340-2354

——, ——, ——, and F. J. Wentz, 2005. High-Resolution Satellite Measurements of the Atmospheric Boundary Layer Response to SST Variations along the Agulhas Return Current. *J. Climate*, 18, 2706-2723

Parthasarathy, B., A. A. Munot, and D. R. Kothawale, 1995. Monthly and seasonal rainfall series for All-India homogeneous regions and meteorological subdivisions: 1871-1994. *Contributions from Indian Institute of Tropical Meteorolgy*, Research Report RR-065, August 1995, Pune 411 008 India

Pearce, A. F., 1980. Early observations and historical notes on the Agulhas Current circulation. *Trans. Roy. Soc. South Africa*, 44(P2), 205-212

Petersen, G. N., J. E. Kristjánsson, and H. Ólafsson, 2004. Numerical simulations of Greenland's impact on the Northern Hemisphere winter circulation. *Tellus*, 56A, 102-111

Pickart, R. S., M. A. Spall, M. H. Ribergaard, G. W. K. Moore, and R. F. Milliff, 2003. Deep convection in the Irminger Sea forced by the Greenland tip jet. *Nature*, 424, 152-156

Ramage, C. S., 1971. Monsoon Meteorology. International Geophysics Series. Vol. 15, Academic Press, San Diego, CA, pp. 296

Rasmusson, E. M., and T. H. Carpenter, 1982. Variations in tropical sea surface temperature and surface wind fields associated with the Southern Oscillation/El Niño. *Mon. Wea. Rev.,* 110, 354-384

Reason, C. J. C., R. J. Allan, J. A. Lindesay, and T. J. Ansell, 2000. ENSO and climatic signals across the Indian Ocean Basin in the global context. Part I: Interannual composite patterns. *Int. J. Climatol.*, 20, 1285-1327

Riehl, H., 1979. Climate and Weather in the Tropics, Academic Press, London, pp. 611

Romero-Centeno, R., J. Zavala-Hidalgo, A. Gallegos, and J. J. O'Brien, 2003. Isthmus of Tehuantepec wind climatology and ENSO signal, *J. Climate*, 16, 2628-2639

Roper, W., 2004. Geospatial Informatics Applications for Disaster Management. 36th Joint Meeting Panel on Wind and Seismic Effects, Japan. http://www.pwri.go.jp/eng/ujnr/joint/36/36ag.htm

Samelson, R. M., E. D. Skyllingstad, D. B. Chelton, S. K. Esbensen, L. W. O'Neill, and N. Thum, 2005. A note on the coupling of wind stress and sea surface temperature. *J. Climate*, Accepted

Sanderson, W. G., C. Tiercelin, and J. Villanueva, 2001. Accident of the oil tanker "Jessica" off the Galapagos Islands (Ecuador) January 16, 2001: Final Report to European Commission. http://europa.eu.int/comm/environment/civil/marin/reports_publications/jessica_report.pdf

Schlax, M. G., D. B. Chelton, and M. H. Freilich, 2001. Sampling errors in wind fields constructed from single and tandem scatterometer datasets. *J. Atmos. Oceanic Tech*., 18, 1014-1036

Schott, F. A., J. Fischer, U. Garternicht, and D. Quadfasel, 1997. Summer monsoon response of the Northern Somali Current, 1995. *Geophys*. *Res*. *Lett*., 24, 2565-2568

——, and J. P. McCreary Jr., 2001. The monsoon circulation of the Indian Ocean. *Prog*. *Oceanogr*., 51, 1-123

Schultz, D. M., W. E. Bracken, L. F. Bosart, G. J. Hakim, M. A. Bedrick, M. J. Dickinson, and K. R. Tyle, 1997. The 1993 superstorm cold surge: Frontal structure, gap flow, and tropical impact, *Mon. Wea*. *Rev*., 125, 5-39

da Silva, A. M., C. C. Young, and S. Levitus, 1994. Atlas of Surface Marine Data 1994, Volume 1: Algorithms and Procedures. NOAA Atlas NESDIS 6. U.S. Department of Commerce, NOAA, NESDIS

Simpson, G. C., 1921. The South-West Monsoon. *Quart*. *J*. *Roy*. *Meteor*. *Soc*. *London*, 47(199), 151-172

Small, J. R., S.-P. Xie, Y. Wang, S. K. Esbensen, and D. Vickers, 2005. Numerical simulation of boundary layer structure and cross-equatorial flow in the eastern Pacific. *J*. *Atmos*. *Sci*., 62, 1812-1830

Stewart, R. H., 2005. Introduction to Physical Oceanography. Online textbook, http://oceanworld.tamu.edu/resources/ocng_textbook/contents.html. Chap. 9

Stramma, L., and J. R. E. Lutjeharms, 1997. The flow field of the subtropical gyre in the South Indian Ocean. *J. Geophys. Res.*, 102, 5513-5530

Stumpf, H. G., 1975. Satellite detection of upwelling in the Gulf of Tehuantepec, Mexico. *Mar. Wea. Log*, 19, 71-74

Sweet, W. R., R. Fett, J. Kerling, and P. LaViolette, 1981. Air–sea interaction effects in the lower troposphere across the north wall of the Gulf Stream. *Mon. Wea. Rev.,* 109, 1042-1052

Trasviña, A., E. D. Barton, J. Brown, H. S. Velez, P. M. Kosro, and R. L. Smith, 1995. Offshore wind forcing in the Gulf of Tehuantepec, Mexico: The asymmetric circulation. *J. Geophys. Res.*, 100, 20,649-20,663

Wallace, J. M., T. P. Mitchell, and C. Deser, 1989. The influence of sea surface temperature on surface wind in the eastern equatorial Pacific: Seasonal and interannual variability. *J. Climate*, 2, 1492-1499

Webster, P. J., V. O. Magaña, T. N. Palmer, J. Shukla, R. A. Thomas, M. Yanai, and T. Yasunari, 1998. Monsoons: Processes, predictability, and the prospects for prediction, *J. Geophys. Res.*, 103, 14,451-14,510

Weeks, S. J., F. A. Shillington, and G. B. Brundrit, 1998. Seasonal and spatial SST variability in the Agulhas retroflection and Agulhas return current. *Deep-Sea Res.*, 45, 1611-1625

Xie, S.-P., 2004. Satellite observations of cool ocean-atmosphere interaction. *Bull. Amer. Meteor. Soc.*, 85, 195-208

——, X. Haiming, W. S. Kessler, and M. Nonaka, 2005. Air–Sea Interaction over the Eastern Pacific Warm Pool: Gap Winds, Thermocline Dome, and Atmospheric Convection. *J. Climate*, 18(1), 5-20

Yanai, M., C. Li, and Z. Song, 1992. Seasonal heating of the Tibetan Plateau and its effects on the evolution of the Asian summer monsoon. *J. Meteor. Soc. Japan*, 70, 319-351

Appendix A: List of Acronyms

ARC	Agulhas Return Current
AIRI	All-India Rainfall Index
ASCII	American Standard Code for Information Interchange
AVHRR	Advanced Very High Resolution Radiometer
COADS	Comprehensive Ocean-Atmosphere Data Set
COGOW	Climatology of Global Ocean Winds
DEC	Digital Equipment Corporation
DPI	Dots Per Inch
EA	Environmental Assessment
EIS	Environmental Impact Statement
ENSO	El Niño Southern Oscillation
FONSI	Finding of no Significant Impact
IPIECA	International Petroleum Industry Environmental Conservation Association
ITCZ	Inter-Tropical Convergence Zone
LLJ	Low Level Jet
MABL	Marine Atmospheric Boundary Layer
MODIS	The Moderate Resolution Imaging Spectroradiometer
NaN	Not a Number
NAO	North Atlantic Oscillation
NASA	National Aeronautics and Space Agency
NCAR	National Center for Atmospheric Research
NCDC	National Climatic Data Center
NCEP	National Centers for Environmental Predication
NDBC	National Data Buoy Center
NEPA	National Environmental Policy Act
NMOSCP	National Marine Oil Spill Contingency Plan
NOAA	National Oceanic and Atmospheric Administration
NRT	Near Real-Time
NSRI	National Sea Rescue Institute
NWS	National Weather Service
OR&R	Office of Response and Restoration
PDO	Pacific Decadal Oscillation
PORTS	Physical Oceanographic Real Time System
SAR	Search and Rescue

SeaWiFS	Sea-viewing Wide Field-of-view Sensor
SLP	Sea Level Pressure
SST	Sea Surface Temperature
TAO	Tropical Atmosphere Ocean
TCZ	Tropical Convergence Zone
URL	Uniform Resource Locator

Appendix B: Raw Data Used to Create the July (2000-2004) Wind Rose Plot for the 0.5° x 0.5° grid cell centered at 39.75°N 125.75°W

QuikSCAT Daily Observations (July 2000-2004)
39.75N_234.25E
01July00,19.8,171.4
02July00,17.2,166.1
03July00,16.3,162.8
04July00,19.4,163.9
05July00,24.3,168.8
06July00,28.0,173.6
07July00,29.5,174.0
08July00,30.5,172.5
09July00,27.5,169.9
10July00,23.3,167.2
11July00,18.6,163.9
12July00,18.3,158.2
13July00,16.7,156.8
14July00,14.6,157.5
15July00,10.7,156.4
16July00,7.2,151.1
17July00,4.6,78.8
18July00,5.6,52.5
19July00,5.6,36.0
20July00,8.8,114.8
21July00,13.8,157.5
22July00,18.1,163.9
23July00,21.9,166.1
24July00,19.5,167.6
25July00,18.8,171.0
26July00,20.5,175.5
27July00,25.3,175.5
28July00,26.6,174.8
29July00,23.6,174.8
30July00,21.9,174.0
31July00,20.8,168.4
01July01,21.6,169.1
02July01,21.7,167.2
03July01,21.9,163.1
04July01,22.1,160.5
05July01,17.1,157.5
06July01,13.5,156.8
07July01,9.6,150.0
08July01,NaN,NaN
09July01,16.0,164.6
10July01,21.2,168.8
11July01,23.9,171.0
12July01,25.7,172.9
13July01,21.7,177.0
14July01,19.4,175.5
15July01,17.8,171.0
16July01,20.0,162.8
17July01,18.1,157.5
18July01,15.8,159.0
19July01,11.5,156.0
20July01,17.1,160.9
21July01,20.7,161.6
22July01,19.3,159.8
23July01,18.2,160.1
24July01,18.9,158.6
25July01,20.6,165.8
26July01,18.9,168.0
27July01,15.3,171.0
28July01,12.4,157.1
29July01,13.6,156.4
30July01,16.5,162.8
31July01,18.4,166.5
01July02,15.5,166.1
02July02,16.9,165.8
03July02,19.3,160.9
04July02,22.1,160.1
05July02,25.4,163.9
06July02,25.8,166.5
07July02,26.4,168.4
08July02,26.4,168.4
09July02,19.6,182.2
10July02,17.9,179.6
11July02,15.8,175.1
12July02,14.9,167.6

13July02,16.3,166.1
14July02,18.1,165.0
15July02,20.6,162.4
16July02,19.6,160.1
17July02,19.0,159.4
18July02,16.3,156.4
19July02,16.5,153.8
20July02,15.8,158.2
21July02,15.9,159.8
22July02,15.9,162.4
23July02,19.6,164.2
24July02,24.3,170.6
25July02,25.9,175.5
26July02,25.8,177.4
27July02,27.5,175.9
28July02,27.3,173.6
29July02,26.7,170.2
30July02,20.8,159.8
31July02,18.9,154.1
01July03,11.6,150.0
02July03,20.0,168.4
03July03,26.3,171.0
04July03,24.8,169.5
05July03,22.0,166.5
06July03,16.0,160.1
07July03,10.8,144.8
08July03,9.2,142.5
09July03,12.6,150.8
10July03,17.5,156.4
11July03,22.3,162.4
12July03,22.8,166.9
13July03,22.2,168.4
14July03,20.8,166.1
15July03,21.1,164.6
16July03,21.3,163.5
17July03,19.2,162.8
18July03,15.5,153.0
19July03,15.2,154.9
20July03,18.4,156.8
21July03,21.4,165.0
22July03,18.6,174.8
23July03,10.2,195.0
24July03,6.0,227.6
25July03,4.2,241.1
26July03,11.7,170.6
27July03,22.5,172.5
28July03,23.6,172.9
29July03,21.5,177.0
30July03,15.9,184.9
31July03,17.3,186.4
01July04,13.7,117.0
02July04,16.9,160.1
03July04,22.0,172.5
04July04,22.8,173.2
05July04,23.3,174.8
06July04,21.8,167.2
07July04,19.7,166.1
08July04,17.0,160.1
09July04,14.9,158.6
10July04,11.3,134.6
11July04,9.7,140.2
12July04,8.2,135.8
13July04,9.5,139.5
14July04,12.2,138.8
15July04,15.6,153.0
16July04,18.6,162.4
17July04,20.7,166.1
18July04,21.8,165.8
19July04,21.4,165.0
20July04,20.0,166.1
21July04,19.6,163.1
22July04,21.6,168.0
23July04,25.5,171.4
24July04,26.9,172.1
25July04,27.7,169.5
26July04,25.8,167.6
27July04,24.6,171.8
28July04,23.9,173.2
29July04,23.0,174.0
30July04,21.7,169.1
31July04,21.6,174.0